FESOM2.1-REcoM3-MEDUSA2: an ocean-sea ice-biogeochemistry model coupled to a sediment model

Ying Ye[1], Guy Munhoven[2], Peter Köhler[1], Martin Butzin[1,3], Judith Hauck[1], Özgür Gürses[1], and Christoph Völker[1]

[1]Alfred-Wegener-Institut Helmholtz-Zentrum für Polar- und Meeresforschung (AWI), P.O. Box 12 01 61, 27515 Bremerhaven, Germany
[2]Laboratoire de Physique Atmosphérique et Planétaire, Université de Liège, B–4000 Liège, Belgium
[3]MARUM — Center for Marine Environmental Sciences, University of Bremen, Bremen, Germany

Correspondence: Ying Ye (Ying.Ye@awi.de)

Abstract.

This study describes the coupling of the process-based Model of Early Diagenesis in the Upper Sediment (MEDUSA version 2) to an existing ocean biogeochemistry model consisting of the Finite-volumE Sea ice-Ocean Model (FESOM version 2.1) and the Regulated Ecosystem Model (REcoM version 3) with flexible stoichiometry of organic matter. Atmospheric CO_2 in the model is a prognostic variable which is determined by the carbonate chemistry in the surface ocean. The model setup and its application to a pre-industrial control climate state is described in detail. In the coupled model, 550 PgC are stored in the top 10 cm of the bioturbated sediment, mainly as calcite, but also to 12% as organic matter. Simulated atmospheric CO_2 reached 282 ppm after 2000 years of the coupled simulation, which is close to the initially assumed value of the pre-industrial CO_2 level. Sediment burial of carbon, alkalinity and nutrients in the coupled simulation is set to be partly compensated by riverine input. The spatial distribution of biological production is altered depending on the location of riverine nutrient input, the changes in sedimentary input as well as the strength of local nutrient limitation, while the global productivity is not affected substantially.

1 Introduction

The ocean plays a key role in the global carbon cycle. It stores about 37,200 PgC (Keppler et al., 2020), more than 40 times as much carbon as the atmosphere, which contained 884 PgC (or 417 ppm) in the year 2022 (Lan et al., 2023). About 25–30% of the global anthropogenic CO_2 emissions are taken up by the world oceans (Friedlingstein et al., 2022).

CO_2 enters the ocean through gas-exchange, where it dissolves in seawater. A unique feature of dissolved CO_2 is that it reacts with water to form carbonic acid (H_2CO_3), which is instable and dissociates as a function of temperature, salinity and pressure into bicarbonate (HCO_3^-), carbonate (CO_3^{2-}) and hydrogen (H^+) ions (Zeebe and Wolf-Gladrow, 2001). The dissolved inorganic carbon (DIC), which is the sum of CO_2, HCO_3^- and CO_3^{2-}, is distributed in the ocean via circulation. Part of the carbon in the surface ocean is also taken up via photosynthesis by marine phytoplankton and exported into the ocean interior via the sinking of dead organic matter. When stored in the deep ocean, this carbon reduces the surface concentration of

DIC and allows for further CO_2 uptake from the atmosphere. Another important process in the marine carbon cycle is driven by calcifying plankton. These organisms produce calcium carbonate ($CaCO_3$) shells whereby CO_2 is released back into the atmosphere. These processes which all influence the surface-to-depth-gradient in DIC are also summarized as the so-called marine carbon pumps (Volk and Hoffert, 1985). Some of the particulate carbon (i.e., particulate organic carbon and $CaCO_3$, ca. 1% of primary production; Sarmiento and Gruber, 2006) escapes dissolution and remineralization in the water column and sinks to the seafloor, where it might be buried. These particles are then removed from the relatively fast cycling of carbon at the surface of the Earth.

The storage of carbon, alkalinity and nutrients in sediments introduces an additional slow timescale to carbon cycling, and overall increases the carbon storage in the sediment-ocean system. The global burial flux of particulate organic carbon (POC) in marine sediments has been reported to be in a range of 160–2600 $\mathrm{PgC\,kyr^{-1}}$ (Burdige, 2007; Dunne et al., 2007; Sarmiento and Gruber, 2006; Muller-Karger et al., 2005). In total $\sim$280 $\mathrm{PgC\,kyr^{-1}}$ are buried as $CaCO_3$ in marine sediments of which 100–150 $\mathrm{PgC\,kyr^{-1}}$ find their way into sediments of the deep-sea below at least 1 km of water depth (Sarmiento and Gruber, 2006; Dunne et al., 2012; Cartapanis et al., 2018; Hayes et al., 2021).

Furthermore, marine sediments play an important role as they provide records of the Earth's past climate. They react via the carbonate compensation feedback to any changes in the marine carbon cycle, in which the deep ocean carbonate ion concentration is brought back to its initial values after a perturbation on a multi-millennial timescale via sediment dissolution of $CaCO_3$ (Broecker and Peng, 1987).

Anthropogenic carbon emissions represent a rapid carbon cycle perturbation and in high-emission scenarios (Meinshausen et al., 2011), may ultimately lead to the massive dissolution of $CaCO_3$ in seafloor sediments over the next millennia (Archer et al., 1997). This carbonate compensation feedback contributes to a reduction of the long-term airborne fraction of anthropogenically emitted CO_2 from more than 20% if only the atmosphere-ocean is considered to be less than 10% (Archer et al., 2009; Köhler, 2020). This additional oceanic uptake of anthropogenic carbon through the dissolution of $CaCO_3$, however, operates on a multi-millennial timescale, and is therefore only of interest for the geological fate of fossil emissions, but not for our near future. Hence, understanding processes controlling the sediment-ocean exchange and quantifying the carbon storage in marine sediments are crucial to explain transient behaviour over changing climates, e.g. the glacial-interglacial CO_2 variations (e.g. Brovkin et al., 2012; Köhler and Munhoven, 2020), and to predict the long-term ocean sequestration of anthropogenic carbon (Archer et al., 2009; Köhler, 2020).

All ocean biogeochemistry models incorporate a scheme to describe the fate of biogenic material that reaches the seafloor, but differ in their complexity (Munhoven, 2021, and references therein). The most simple schemes start from a reflective boundary condition, where all material reaching the seafloor is remineralized and returned to solution. More complex schemes consider a single, vertically integrated mixed-layer sediment box with a complete mass balances for the particles settling to the seafloor. Even higher complexity is found in vertically resolved sediment models describing diagenetic reactions, mechanical changes of dissolved and solid components as well as burial fluxes out of the surface sediment.

FESOM2.1-REcoM3, consisting of the Finite-volumE Sea ice-Ocean Model 2.1 and the Regulated Ecosystem Model 3, is one of the ocean biogeochemistry models, which so far includes a simple one-layer sediment model (Gürses et al., 2023). RE-

coM3 describes the marine ecosystem at medium complexity with two phytoplankton classes including silicifiers and calcifiers, two zooplankton classes representing mixed zooplankton and polar macrozooplankton, and considers flexible stoichiometry of C, N, Si, Fe, $CaCO_3$, and chlorophyll. Various iron sources (sediment, dust and rivers) are implemented into REcoM3 and the model also has the option to simulate the cycles of ^{13}C and ^{14}C (Butzin et al., 2023). The sediment layer used so far in REcoM3 ensures the mass conservation by a complete remineralization of material sinking into the sediment. It represents processes in the surface sediment and is useful for short-term simulations, since the characteristic time scales of early diagenetic processes are often of the order of days to months, while long-term burial via sedimentation (which compensates riverine inputs from continental weathering) acts on time scales of thousands of years. Kriest and Oschlies (2013) have shown that the introduction of a sediment box makes models more robust against the uncertainties of the remineralization length scale, compared to models that remineralize everything in the water column. However, without considering sediment-ocean fluxes and feedbacks in more detail the model would not be able to reasonably simulate transient changes over glacial/interglacial timescales.

In Sect. 2, we describe the coupling of FESOM2.1-REcoM3p, a model configuration targeted for paleo-application, with MEDUSA2, the Model of Early Diagenesis in the Upper Sediment (Munhoven, 2021). MEDUSA2 is a process-based sediment module that offers a complex alternative to the previously used simple one-layer sediment. This is the first realisation of such an ocean-sediment setup of the marine carbon cycle with flexible stoichiometry of organic matter. In comparable existing alternatives (e.g. Kurahashi-Nakamura et al., 2020; Moreira Martinez et al., 2016) stochiometry was kept fixed. This feature enables our model to simulate the growth limitation and community composition of phytoplankton in a more realistic way so that the biological carbon pump has a higher flexibility to react to climate change (Seifert et al., 2022; Schartau et al., 2007; Hohn, 2009). The final model configuration, referred to as FESOM2.1-REcoM3p-MEDUSA2, is applicable to relevant questions in paleoclimate research and should be able to provide new insights into the long-term dynamics of the marine carbon cycle. The coupled ocean-sediment simulation of this configuration under pre-industrial climate conditions is analysed in Sect. 3, while its applications to question of the last glacial cycle are envisaged in future, more targeted studies.

2 Methods

2.1 Model description

2.1.1 REcoM3p – A REcoM3 configuration for paleo research

REcoM is an ocean biogeochemistry and ecosystem model describing cycles of carbon, oxygen and nutrients (nitrogen, silicon and iron) with varying intracellular stoichiometry in phytoplankton, zooplankton and detritus. REcoM3 is the most recent release version and a detailed description of this version including its coupling to FESOM2.1 is given by Gürses et al. (2023). The configuration REcoM3p used here has on the one hand reduced complexity with respect to functional groups of the modelled ecosystem and considered only one generic zooplankton and one detritus class, instead of two in the full version of REcoM3 (Fig. 1). As in the full version, diatoms and small phytoplankton which include calcifiers (only calcite producers, no aragonite) are considered here. The total 22 biogeochemical tracers cover nutrients (dissolved inorganic nitrogen DIN,

dissolved silicate DSi and dissolved iron DFe), two types of phytoplankton (diatoms and small phytoplankton) with the state variables C, N and chlorophyll, as well as biogenic silica in diatoms and calcite in small phytoplankton, one zooplankton with C and N pools, one detritus with the state variables C, N, calcite and opal, dissolved organic matter with C and N pools, dissolved inorganic carbon (DIC), alkalinity (Alk) and oxygen (O_2). The biological cycling of iron is described using a fixed Fe:N ratio in phytoplankton, zooplankton and detritus. The same parameter values were used as described in Gürses et al. (2023) and only two parameters were tuned for the reduced food web and coarser resolution (Tab. D1).

So far REcoM3 only included a single-layer sediment. Particles sinking out of the bottom water boxes enter this sediment layer and go through remineralization (organic particles) and dissolution (calcite and opal) following a simple first-order decay approach: organic matter remineralization is neither dependent on O_2 availability nor does it follow different redox pathways; carbonate dissolution proceeds irrespective of the ambient saturation state (similarly to the dissolution in the water column). The approach is thus equivalent to a classical reflective boundary with temporal buffering. The fluxes of solutes back to the bottom water boxes are derived from the remineralization and dissolution rates of the solids via the elemental ratios that characterize them. While the main aim of this study is the replacement of this simple sediment with the more complex sediment representation of the MEDUSA2 model, we keep this configuration as an alternative option for comparisons (labelled R_{sedbox} – see Sect. 2.4 below).

On the other hand, REcoM3p contains some extensions of relevance for the planned paleo applications when compared to the version described by Gürses et al. (2023): First, atmospheric CO_2 concentrations are calculated assuming that the atmosphere can be represented as a homogeneous carbon reservoir. The carbon cycle on land (continental biosphere) is not considered. Temporal changes in the atmospheric volume mixing ratio of CO_2 (X_{CO_2}, in ppm) then solely result from the globally integrated air-sea CO_2 flux, given by

$$\frac{\delta X_{CO_2}}{\delta t} = -\frac{\rho_{air}}{m_{atm}} \cdot 10^6 \int F_{CO_2}\, dA,$$

where F_{CO_2} ($mol\, m^{-2}\, s^{-1}$) is the regional air-sea CO_2 flux (calculated according to Wanninkhof (2014)), dA integrates over the ocean area, $\rho_{air} = 0.02897\, kg\, mol^{-1}$ is the molar mass of dry air (from Picard et al. (2008), rounded here to four significant figures) and $m_{atm} = 5.1352 \cdot 10^{18}\, kg$ is the mass of the dry atmosphere (Trenberth and Smith, 2005). The factor 10^6 serves to convert from mol fractions to ppm.

Second, a riverine source of DFe was added to the already existing two sources from dust and marine sediments. Furthermore, due to the coupling to MEDUSA2, the sedimentary source of iron can be calculated in two ways: 1) in a fixed ratio to degradation of particulate organic nitrogen (PON) in the benthic layer as described in Gürses et al. (2023, Eq. A67 in Appendix A); 2) in a fixed ratio to the diffusive flux of DIN calculated by MEDUSA2 in the coupled simulations. Elrod et al. (2004) demonstrated a clear correlation between the iron flux out of sediments and the oxidation of organic matter on shelves, with a Fe : N ratio that is much higher than typical Fe : N ratios in sinking organic matter. Under anoxic conditions in sediments, the flux of iron is increased due to the greater solubility of ferrous iron. To represent this effect, we applied a higher Fe : N ratio (3 µmol Fe : 20 mmol N) for the flux of iron from the sediment to the water column than the ratio of 1 µmol Fe : 30 mmol N that
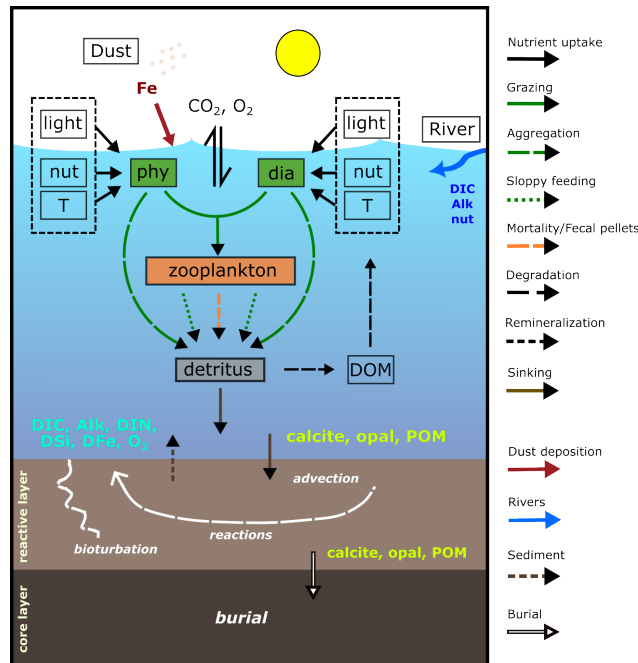
Figure 1. Schematic diagram of the components and interactions in REcoM3p coupled with the sediment model MEDUSA2 (modified and extended from Gürses et al. (2023, Fig. 2)). Small phytoplankton (**phy**) and diatoms (**dia**) take up inorganic nutrients (**nut**) and grow in dependence on **light** and temperature (**T**). One generic **zooplankton** consumes phytoplankton. Phytoplankton aggregation, zooplankton sloppy feeding, mortality and fecal pellets generate sinking **detritus**. Sinking detritus degrades to dissolved organic matter (**DOM**) which then remineralizes to dissolved inorganic carbon (DIC) and nitrogen (DIN). **Calcite**, **opal** and particulate organic matter (**POM**) reaching the seafloor enter the reactive layer of sediments, where accumulation, bioturbation, degradation and dissolution take place. Dissolved products of these processes (**DIC, Alk, DIN, DSi, DFe and O_2**) go back to the bottom water by diffusion. The solids accumulate and are buried further in the core layer. Sources of DIC, Alk and nutrients to the ocean include sediments and rivers and dust deposition is an additional source of iron.

we used for remineralization in the water column. The same $\mathrm{Fe : N}$ ratio is used for both methods to calculate the sedimentary input of iron. A comparison of source strengths for iron is discussed in Sect. 3.2.

125   Third, carbon isotopes were recently implemented into REcoM3p, as described in Butzin et al. (2023). However, the implementation of carbon isotopes into MEDUSA2 is not yet finished, which is why we here use REcoM3p with carbon isotopes switched off.

2.1.2   The sediment model MEDUSA2

MEDUSA is a time-dependent one-dimensional numerical model of coupled early diagenetic processes in sea-floor surface
130   sediments. The original model version (MEDUSA v1) was described in Munhoven (2007). MEDUSA v1 has evolved to become MEDUSA2 which allows for a flexible chemical composition of the sediment, of the network of chemical transfor-

mations that describe the diagenetic processes (e.g. denitrification, etc.), and chemical equilibria to consider. It also offers a variety of Application Programming Interfaces (APIs) for coupling it to ocean models with different grid configurations and biogeochemical components (Munhoven, 2021).

135   In MEDUSA a sediment column is divided into three realms (the optional fourth one, a Diffusive Boundary Layer at the sediment-water-interface was not considered here). The topmost part from the sediment surface is called REACLAY and encompasses the reactive mixed-layer where solids sinking from the bottom layer of the ocean are collected. This is where chemical reactions take place, solids are transported by bioturbation and advection resulting from the continuous deposition of new material, and solutes by molecular diffusion. The second major realm is the located underneath, and is called CORELAY.

140   It is made of a stack of sediment layers, typically 1 cm thick each. Here, no reactions or mixing take place: solids are buried and preserved in this realm which is building up a synthetic sediment core. REACLAY and CORELAY are connected by an thin transitional layer (TRANLAY) which acts as a short-term (numerical) storage buffer and which can also be seen as the topmost layer of CORELAY. In our coupled configuration MEDUSA2 sediment columns (one per seafloor grid element) only resolve a 10 cm thick reactive surface sediment layer on a vertical grid with 21 points. The grid point spacing is not regular but

145   increases with depth in the sediment in order to allow for a better representation of the strong subsurface solute concentration gradients. The burial flux from the reactive layer into the core layer were monitored in our simulations, but not the changes of solids in the core layer. There is no lateral exchange between sediment columns.

MEDUSA has already been coupled to several ocean biogeochemistry and Earth System Models (Moreira Martinez et al., 2016; Kurahashi-Nakamura et al., 2020; Munhoven, 2021). Coupling to ocean models is done through so-called 'applica-

150   tions' in the MEDUSA code. We introduced a new application `medusa-fesom-recom` which controls 1) the reading of FESOM2.1-REcoM3p input and conversion into format and units that MEDUSA requires, 2) the selection of processes and global rate parameter values for tracing the evolution of the concentrations of solids and solutes considered, and 3) the writing of the resulting diffusive solute exchange with the ocean to a file for usage by FESOM2.1-REcoM3p and the obtained burial loss of solids into the sediment core. These burial losses can be used to monitor and/or regulate oceanic mass balances of

155   carbon, alkalinity and the main nutrients (nitrogen and silicon).

Consistent with the input from FESOM2.1-REcoM3p, we chose a MEDUSA2 configuration with five solids (clay, calcite, opal and two types of organic matter) and six solute components (CO_2, HCO_3^-, CO_3^{2-}, O_2, NO_3^- and H_4SiO_4). The two types of organic matter are needed to account for the variable stoichiometry in REcoM3p. Processes altering the content of solids and solutes in sediments include calcite dissolution, oxic respiration of organic matter, organic matter degradation by

160   denitrification, opal dissolution, and chemical equilibria of the carbonate system in the porewaters. REcoM3p only calculates formation and dissolution of calcite and does not represent aragonite. Correspondingly, only calcite dissolution in sediments is considered in the MEDUSA2 application `medusa-fesom-recom`.

As mentioned above, in the model setup organic matter can get degraded through oxidation by either oxygen or via denitri-fication, i.e., organic matter is preserved and buried once it reaches a sediment depth which is devoid of O_2 and NO_3^-. This

165   may result in too high preservation rates of organic matter in shallow shelf regions with high input rates of organic matter. Be-yond nitrate, MEDUSA2 has previously been used with coupled Mn and Fe reduction and oxidation cycles (Munhoven, 2021).

Sulfate reduction could also be easily added as a further oxidative pathway for organic matter. These additional degradation pathways are, however, not considered here, as including these processes requires a much finer vertical resolution and deeper reaching columns in the sediment model (e.g., 340 nodes instead of 21 in the JEASIM application in Munhoven, 2021).

Biological components in REcoM3p have variable intracellular stoichiometry and thus the seafloor deposition fluxes of POC and PON (particulate organic nitrogen) have no fixed ratio. However, in MEDUSA2 degradation of particulate organic matters (POM) is calculated for POM classes with a fixed stoichiometry each. We therefore defined two end-member classes of POM in MEDUSA2 in which $Q = C : N$ is fixed with $Q_1 = 106 : 21$ and $Q_2 = 200 : 11$, respectively, representing the minimum and maximum C:N ratio simulated in the seafloor deposition flux in REcoM3p. The total outgoing fluxes of PON from REcoM3p (F_N^o) were then partitioned into two incoming contributions F_N^{i1} and F_N^{i2}, according to

$$F_N^{i1} = \frac{Q_2 - Q}{Q_2 - Q_1} \cdot F_N^o \tag{1}$$

$$F_N^{i2} = \frac{Q - Q_1}{Q_2 - Q_1} \cdot F_N^o \tag{2}$$

where $Q = F_C^o / F_N^o$ is the ratio of the bulk POC flux (F_C^o) to the PON flux (F_N^o) that reaches the seafloor in REcoM3p. The carbon fluxes carried by the two POM classes are finally calculated by multiplying the nitrogen fluxes F_N^{i1} and F_N^{i2} with the respective $C : N$ ratios:

$$F_C^{i1} = Q_1 \cdot F_N^{i1} \tag{3}$$

$$F_C^{i2} = Q_2 \cdot F_N^{i2} \tag{4}$$

The degradation time scale of organic matter depends on its elemental composition (i.e. the $C : N$ ratio) (Amon and Benner, 1994; Martin et al., 1987). In the water column in FESOM2.1-REcoM3p, we considered a faster remineralization of nitrogen compared to carbon with the ratio of 1.1:1 (ρ_{DetN} and ρ_{DetC} in Gürses et al. (2023), Tab. A8). The rate law expression chosen for the oxic degradation of organic matter in the sediment is more complex: it is linear in the concentration of organic matter in porewaters (with separate expressions for $[POM_1]$ and $[POM_2]$), and includes a Monod-type (hyperbolic) limitation with respect to the concentration of oxygen in the porewaters ($[O_2]$ – see Tab. D2 for details). Based on tuning experiments for a better representation of the sediment POC content, we adopted a 10-fold faster degradation rate for the low-C:N organic matter class (k_{ox1} for POM_1) than for the high-C:N organic matter class (k_{ox2} for POM_2).

Besides organic matter, calcite and opal, the simulated sediment contains an inert component, which we refer to as 'clay' here for the sake of simplicity, and which is ultimately of continental origin. It stems from dust particles deposited over the sea surface and from terrestrial materials transported to the oceans by rivers. In our model setup, annual mean dust deposition from Albani et al. (2014) is considered as the oceanic clay input into sediments. Further, a globally constant input of $2.5 \cdot 10^{-8} \, mol \, illite \, cm^{-2} \, year^{-1}$ over the seafloor (10-fold higher than Heinze et al. (1999) based on tuning experiments) was added, assuming that clay has the composition of illite. This uniform flux is meant to represent the terrestrial component in clay which is redistributed by ocean internal processes, such as mixing and resuspension. The strength of this flux is a result of tuning experiments and the total clay input is shown in Fig. A1.

2.2 Coupling REcoM3p and MEDUSA2

FESOM2.1-REcoM3p and MEDUSA2 are sequentially coupled through file exchange. Sinking fluxes of POC, PON, opal (SiO_2) and calcite out of the bottom water boxes are saved as output files by FESOM2.1-REcoM3p and read as input files by MEDUSA2 (Fig. 1). Furthermore, MEDUSA2 requires information on temperature, salinity and concentrations of alkalinity (Alk), DIC, oxygen, and nutrients in the bottom-most ocean model box. Temperature and salinity enter thermodynamic calculations in the sediment model and the bottom water concentrations are used in the calculation of diffusive fluxes between sediment and water column.

FESOM2.1-REcoM3p reads diffusive fluxes of nutrients including dissolved inorganic nitrogen (DIN) and dissolved silicate (DSi or H_4SiO_4), DIC, Alk and oxygen from the MEDUSA2 output file (Fig. 1). DFe input from sediments is derived from the diffusive flux of DIN, using a fixed Fe:N ratio. Other quantities that are calculated by MEDUSA2 are the permanent burial of carbon, organic matter, opal and calcite in the sediment core. This output is used to monitor, and partly compensate, changes in the total mass balances of carbon and the other tracers in the ocean and reactive sediment. For silicon and nitrogen we assumed that riverine input compensates the burial flux, while for Alk, a global riverine input was taken from Börker et al. (2020) representing weathering fluxes. Based on the sediment burial of carbon (POC and calcite, Table 2), we tuned DIC river input to reproduce the pre-industrial CO_2 level. The total riverine input is distributed over the surface ocean in the model by scaling it with the local river runoff from the forcing data.

2.3 Model setup

2.3.1 Model configuration

FESOM2.1 employs unstructured meshes with variable horizontal resolution. The default mesh of FESOM2.1-REcoM3 (COR-EII mesh) has about 127 000 surface nodes with a nominal average resolution of 1 degree and enhanced resolution in the equatorial belt and in high latitudes going up to 25 km (Gürses et al., 2023). For testing the coupling with MEDUSA2 a reduced model resolution (PI mesh) is used here, containing 3140 surface nodes, corresponding to a median horizontal resolution of 260 km (Butzin et al., 2023). This configuration reduces computational costs and simplifies simulations over the time scale of thousands of years in order to approach deep ocean equilibrium and significant changes in marine sediments. MEDUSA2 is coupled to the bottom layers of the ocean model, therefore the horizontal grid within MEDUSA2 is always the same as in the ocean model.

Vertically, the ocean is divided into 47 layers and the layer thickness ranges from 5 m in the surface to 250 m in the deep ocean. The full free-surface formulation (zstar) was used, allowing vertical movement of all layers, to ensure tracer conservation in FESOM (Scholz et al., 2019, 2022). In this study, the model was retuned for the coarser resolution by reducing the maximum thickness diffusivity of the Gent-McWilliams parameterisation from $3000\,\mathrm{m^2\,s^{-1}}$ (used in the default FESOM2.1) to $1000\,\mathrm{m^2\,s^{-1}}$.

2.3.2 Forcing and initial conditions

FESOM2.1 is initialised with seasonal winter temperatures and salinities from the Polar Science Center Hydrographic Climatology (PHC3, updated from Steele et al. (2001)) and driven by annually repeated atmospheric fields using the Corrected Normal Year Forcing Version 2.0 (CORE-NYF.v2, Large and Yeager, 2009).

The initial value of X_{CO_2} is 284.3 ppm following Meinshausen et al. (2017). Alk and DIC are initialised from version 2 of the Global Ocean Data Analysis Project (GLODAPv2) data set (Lauvset et al., 2016), DIN and DSi from the Levitus World Ocean Atlas climatology of 2013 (Garcia et al., 2014) and oxygen from the Levitus World Ocean Atlas climatology of 2018 (Garcia et al., 2019). The initial DFe field is based upon output from the Pelagic Interaction Scheme for Carbon and Ecosystem Studies (PISCES) model (Aumont et al., 2015), as outlined in (Gürses et al., 2023).

Dust input of iron at the sea surface is calculated based on monthly averages of dust deposition by Albani et al. (2014) with a weight percentage for iron of 3.5% and a solubility of 2%. The riverine DFe input is based upon de Baar and de Jong (2001), who estimate that the rivers transport $26\,\mathrm{Gmol\,Fe}$ as DFe to the oceans each year. These authors assume that about 90% of this is lost by flocculation when river water gets mixed with seawater, which reduces the actual input to the ocean to $2.6\,\mathrm{Gmol\,Fe\,yr^{-1}}$. However, depending on types of catchment areas and the concomitant input of organic material which may act as metal chelator, the river input of DFe can be significantly higher (Guieu et al., 1996; Krachler et al., 2005). We therefore tuned our model by varying the river input of DFe (assuming an upper limit of $26\,\mathrm{Gmol\,Fe\,yr^{-1}}$) to get a reasonable distribution of DFe and of the simulated biological productivity, and finally adopted a total riverine DFe input of $5.2\,\mathrm{Gmol\,Fe\,yr^{-1}}$. The river inpur of DFe is distributed at the sea surface by scaling with the river runoff, which is part of the CORE-NYF.v2 forcing.

2.4 Coupled simulation with FESOM2.1-REcoM3p-MEDUSA2

A coupled simulation starts with a spinup FESOM2.1-REcoM3p run (R_{spinup}), followed by the pre-charging of MEDUSA2 (Fig. 2). Subsequently, FESOM2.1-REcoM3p and MEDUSA2 are run alternately with a defined coupling frequency of 50 years ($R_{coupled}$).

2.4.1 FESOM2.1-REcoM3p spinup run (R_{spinup})

FESOM2.1 (without biogeochemistry) was run for 1000 years as a spinup of the ocean circulation. After that, REcoM3p was switched on and run for another 1500 years to get a quasi-equilibrium of deep ocean concentrations. During these 1500 years, the exchange between ocean and sediment was calculated with the alternative one-layer sediment representation. Model output of the last 50 years was analysed as the initial conditions for $R_{coupled}$ in Section 3.1.

2.4.2 Pre-charging of MEDUSA2

Continuous exchange of material between ocean and sediments alters both ocean chemical boundary conditions and the content of the reactive sediment layer. The latter changes much slower due to low sedimentation rates. To reduce the computing time for getting significant changes in sediments, MEDUSA2 was first run for 100,000 years forced by the results from R_{spinup} so
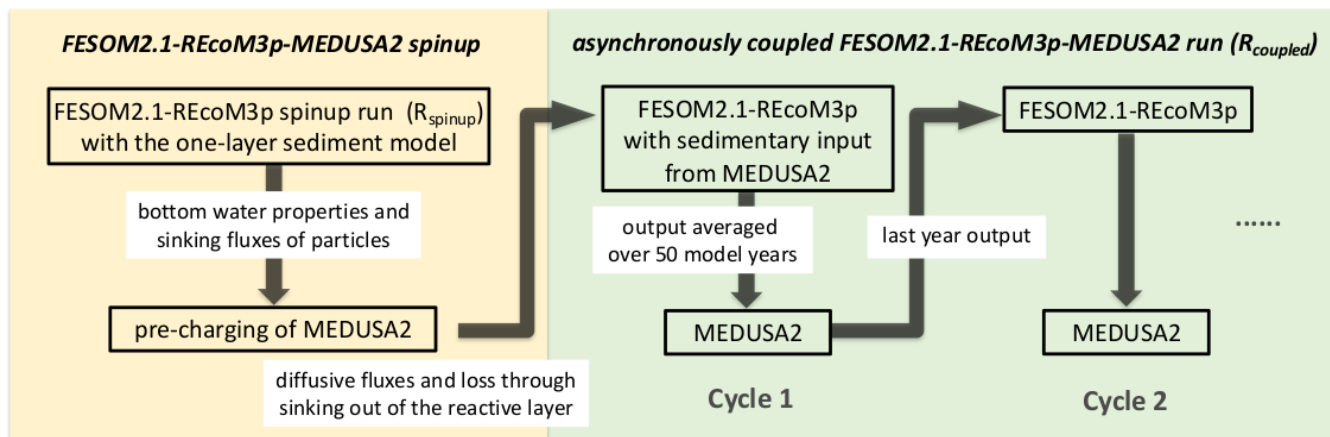
Figure 2. Workflow of a coupled FESOM2.1-REcoM3p-MEDUSA2 simulation.

that the sediment layers in MEDUSA are charged before an interactive coupled FESOM2.1-REcoM3p-MEDUSA2 simulation starts. This way, we may reach an initial seafloor sediment distribution that is as consistent as possible with the productivity pattern, the cycling in the water column and the boundary conditions prevailing at the seafloor (oxygenation, saturation state, etc).

265   2.4.3   Coupled simulation ($R_{coupled}$)

Two simulations were started from the state of year 1500 in R_{spinup} and compared to demonstrate how carbon storage in sediments affects the marine carbon cycle and atmospheric CO_2 (Fig. 2): (1) R_{sedbox} is the continuation of R_{spinup} from year 1500 to year 3500; (2) a coupled simulation $R_{coupled}$ was conducted for 2000 model years starting with the precharged MEDUSA2 sediment layers (see previous section). A coupling frequency of 50 years was consistently applied between FESOM2.1-

270   REcoM3p and MEDUSA2. For each coupling cycle, output of FESOM2.1-REcoM3p was averaged over 50 years before using it as input in MEDUSA2. The sediment-to-ocean fluxes (input to FESOM2.1-REcoM3p) were updated every 50 years with results from the MEDUSA2 simulation. Within one coupling cycle the ocean-sediment exchange fluxes to be applied at each time step were kept constant. The outputs of R_{sedbox} and $R_{coupled}$ were averaged over the last 50 years before comparison (Sect. 3.2).

275   Asynchronous coupling can affect mass conservation in coupled models since the exchange between models is temporally shifted. Here, we quantified this effect in a test simulation. The temporal change of the Si inventory was taken as a measure for mass conservation, since the balance of the silicon cycle is complete in our coupled simulations. The only Si flux out of the ocean-sediment system is the sediment burial of opal and the only input is the riverine flux of DSi into FESOM2.1-REcoM3p which is for mass conservation prescribed by burial flux. Thus, variations in the silicon inventory with time can only be

280   explained by temporal offsets of ocean and sediment processes. An increase of total silicon by about $0.4\%\,\mathrm{kyr}^{-1}$ was observed in the test simulation. Based on this result, a spatially uniform mass correction was applied to bottom water concentrations in

the coupled simulation at the end of each coupling cycle (in our study every 50 model years) so that the total inventory of Si is forced back to that at the beginning of the coupled simulations. The mass correction factor was calculated from the difference between the current inventory and that at the beginning of the coupled simulation. For DIC, Alk, DIN and O_2, corrections were applied with the same correction factor.

2.4.4 Performance of the coupled model

FESOM coupled with REcoM spends about 80% of the total run time of a simulation on the tracer transport computations (Himstedt, 2023). An acceleration method was implemented for a parallel calculation of tracer advection and with two parallel tracer groups on 72 cores, a speedup by a factor of 1.8 was achieved for simulations with the reduced resolution using the PI mesh (Himstedt, 2023). In this study, each coupled FESOM2.1-REcoM3p-MEDUSA2 cycle (50 model years) is then completed within seven hours computation time on 72 cores, of which the MEDUSA2 related calculations require less than five minutes (i.e., of the order of 1% only).

3 Results and Discussion

3.1 FESOM2.1-REcoM3p spinup simulation with the one-layer sediment (R_{spinup})

Generally, the global and basin-averaged profiles of DIC, Alk, DIN, DSi and O_2 in the FESOM2.1-REcoM3p spinup run (R_{spinup}) agree well with GLODAPv2 (Large and Yeager, 2009) and WOA data (Garcia et al., 2019) (Fig. 3), particularly in ocean basins covering large areas of the open ocean. The modelled O_2 concentration in the Arctic Ocean is clearly lower than observed. This will be discussed in Sect. 3.2.5 below.

The global net primary production (NPP) of 35 $PgC\,yr^{-1}$ is lower than the satellite-based estimates but comparable to other modelling studies (see Gürses et al., 2023, Table 3 and references therein), e.g. 24.5–57.3 $PgC\,yr^{-1}$ in CMIP6 (Séférian et al., 2020). The larger part of NPP comes from the small phytoplankton (23 $PgC\,yr^{-1}$); diatoms contribute the remaining 12 $PgC\,yr^{-1}$. Carbon export out of the upper 100 m into the deep ocean is 6.6 $PgC\,yr^{-1}$. The slightly higher productivity and export found here compared to an NPP of 32.5 $PgC\,yr^{-1}$ in the base version of FESOM2.1-REcoM3 (Gürses et al., 2023) can be explained by the differences between the model setups: 1) a much coarser spatial resolution of the PI mesh used here and a different forcing data set, which result in differences in resolved physical processes (e.g., circulation and mixing) and thus in the environmental conditions for phytoplankton growth (e.g., light, temperature and nutrient supply); 2) REcoM3p uses a configuration with a single zooplankton class whereas the simulations in Gürses et al. (2023) contained two zooplankton classes; 3) additional iron input from rivers relieves iron limitation of phytoplankton growth in some regions.

Deposition fluxes from the ocean bottom layer onto the top of the sediments from different simulations and burial fluxes of POC, calcite and opal from the coupled simulation are summarized in Table 1 along with observation-based estimates. The simulated global deposition rate of POC (650 $PgC\,kyr^{-1}$) in R_{sedbox} is lower than the range of observation-based estimates (930–5739 $PgC\,kyr^{-1}$) reported by Burdige (2007). This is not surprising since the global primary and export production in

our model are both lower than observations. The simulated POC deposition rates (Fig. 4a) are in the same order of magnitude as Dunne et al. (2007) but mainly occur on top of deep-sea sediments (deeper than 1 km). The contribution of the deposition rates in shallower waters (37%) underestimates the relative share of 67–82% obtained by others (Muller-Karger et al., 2005; Burdige, 2007). Models with a coarse resolution do not resolve physical processes and thus the biological recycling of carbon in shelf regions well, likely leading to an unrealistic estimation of POC sinking into and accumulation in sediments. This can be clearly seen in a comparison (Tab. 1) with a simulation at higher spatial resolution (R_{high} with 126,858 surface nodes, as in Gürses et al. (2023)). The total POC deposition rate of 850 $PgC\,kyr^{-1}$ comes closer to the estimated range, and the flux in shallower waters represents a larger fraction (80%) of the global flux which falls within the range of estimates (67–82%). Here, we still consider model results with a coarse resolution which is commonly used for technical tests, allowing us to run a reasonable number of tuning experiments and coupled simulations over several thousands of years within a realistic time frame.

A total calcite deposition rate of 380 $PgC\,kyr^{-1}$ is found to reach the ocean-sediment interface in R_{sedbox}, from which 370 $PgC\,kyr^{-1}$ happened in the deep ocean below 1 km water depth. Be aware that the omissions of aragonite and of the benthic production of $CaCO_3$ (e.g., by coral reefs) are important shortcomings of our approach. Buitenhuis et al. (2019) simulated three pelagic calcifiers and estimated a contribution of aragonite producers to shallow water export of $CaCO_3$ at 100 m of at least 33%. Furthermore, coccolithophore and calcifying zooplankton together are reported to contribute to the global carbonate fluxes by 40–60% and the rest of the fluxes remains unexplained (Knecht et al., 2023), which also results in high uncertainty in the simulating calcifying organisms and $CaCO_3$ fluxes. Our model roughly reproduces the spatial pattern of the Th-normalized deposition fluxes (Hayes et al., 2021) with high fluxes in the North Atlantic and Arabian Sea (up to 2 $gC\,cm^{-2}\,kyr^{-1}$), lower fluxes in the main part of the Pacific and Southern Ocean ($< 1\,gC\,cm^{-2}\,kyr^{-1}$, Fig. 4b). Only some parts of the eastern equatorial Pacific region, the modelled calcite fluxes are about two times higher than in Hayes et al. (2021) which might be caused by the too high calcite production in this region in the model.

The seafloor deposition rate of opal in R_{sedbox} is 70 $Tmol\,Si\,yr^{-1}$, of which 65 $Tmol\,Si\,yr^{-1}$ accounted for by those parts of the oceans that are more than 1 km deep. Observation-based estimates show conflicting results with 22–40 $Tmol\,Si\,yr^{-1}$ for the total flux (Dunne et al., 2007; Nelson et al., 1995; Tréguer et al., 1995), while in the ocean that is deeper than 1 km $84 \pm 17\,Tmol\,Si\,yr^{-1}$ (Tréguer and De La Rocha, 2013; Tréguer et al., 2021) should settle. Under the assumption that the newer data are of better quality we can conclude that the simulated opal deposition rates in the deep ocean agree well with reconstructions while for the total rates a revised data set seems necessary. The spatial distribution of opal fluxes agree qualitatively well with Hayes et al. (2021) with high fluxes at high latitudes in both hemispheres and moderate ones along the eastern equatorial Pacific (Fig. 4c). However, the model shows much higher values in the Southern Ocean which indicates that the Fe limitation of diatoms over the Southern ocean in the model is somewhat too weak.

During the total 1500 simulated years the atmospheric CO_2 concentration first rises with time and reaches 289 ppm at the end of R_{spinup} (Fig. 5).

Table 1. Seafloor deposition and burial fluxes of POC ($PgC\,kyr^{-1}$), calcite ($PgC\,kyr^{-1}$) and opal ($Pmol\,Si\,kyr^{-1}$) in simulations and observation-based estimates, reported for the global ocean and ocean regions deeper than 1 km.

	Seafloor deposition					
	POC		calcite		opal	
	global	> 1 km	global	> 1 km	global	> 1 km
R_{sedbox}	650	410	380	370	70	65
$R_{coupled}$	580	390	380	370	80	70
R_{high}	850	160	440	370	45	35
Observed	930–5739[a]	310–1029[b]			22–40[c]	79–84[d]

	Burial					
	POC		calcite		opal	
	global	> 1 km	global	> 1 km	global	> 1 km
$R_{coupled}$	110	50	115	86	82	9.5
Observed	160–2600[e]	2–300[f]	280[g]	100–150[h]	7.1[i]	5.9–9.2[j]

Reference keys: B: Burdige (2007), C16: Cartapanis et al. (2016), C18: Cartapanis et al. (2018), D07: Dunne et al. (2007), D12: Dunne et al. (2012), Ha: Hayes et al. (2021), Hi: Hilton and West (2020), J: Jahnke (1996), M: Muller-Karger et al. (2005), N: Nelson et al. (1995), Sa: Sarmiento et al. (2002), Se: Seiter et al. (2005), T95: Tréguer et al. (1995), T13: Tréguer and De La Rocha (2013), T21: Tréguer et al. (2021).
[a] B, D07, M, Sa; [b] B, J, M, Sa, Se; [c] D07, N, T95; [d] J, T21; [e] B, C18, D07, M; [f] B, C16, C18, D07, Hi, Ha, J, M, Se; [g] C18; [h] C18, D12, Ha, Sa; [i] T95; [j] Ha,T13,T95,T21

3.2 The coupled simulation with FESOM2.1-REcoM3p-MEDUSA2 ($R_{coupled}$)

3.2.1 Sediment content

The weight percentage of sediment composition (Fig. 6) is compared in the following with the data compilation of the surface sediment composition of Hayes et al. (2021), but note that the latter agrees widely with the alternative and much older compilation of Seiter et al. (2004).

Simulated calcite content in $R_{coupled}$ (Fig. 6, row 1) exhibits high values (up to >90%) in the Atlantic, tropical and subtropical South Pacific as well as the Indian Ocean, and lower values (near zero) in the North Pacific and Southern Ocean. Also, the calcite-rich sediments along the Atlantic mid-ocean ridge are reproduced to some extent in the model. This simulated pattern generally agrees well with Hayes et al. (2021).

Opal content (Fig. 6, row 2) is elevated at high latitudes in the North Pacific and North Atlantic Ocean, as well as in the Southern Ocean at the Antarctic Polar Front. This is also seen in the data compilation. The opal distribution mainly reflects the diatom productivity (Fig. 9) and opal deposition rates (Fig. 4). The latter has a similar pattern as ^{230}Th-normalized estimates

by Hayes et al. (2021), whereas much higher fluxes are found in the model over large areas in the Southern Ocean. This could lead to a likely overestimation of opal content in sediments, although not many observations are available for these areas. The opal belt in the equatorial eastern Pacific is smaller and less pronounced in the model than observed. This is related to the somewhat too strong iron limitation of diatoms in this region in our model.

Simulated sediment POC (Fig. 6, row 3) shows a strong contrast between shallow-water regions and open oceans which is not seen in the data compilation. In large areas of the open ocean and low-latitude shallow-water regions, the simulated POC content is negligibly low compared with data, whereas in most of the high-latitude shallow-water regions, it is up to one order of magnitude higher than the measurements. In the eastern equatorial Pacific and the Indian sector of the Southern Ocean the simulated POC has the same order of magnitude as the data compilation. A detailed comparison of POC content in the southern hemisphere, particularly in the South Pacific Ocean, is not possible due to lack of data. Yet in the comparison to Hayes et al. (2021) we found that the simulated deposition rates along the Antarctic coasts are about one order of magnitude higher than the reconstruction, which likely contributes to overestimate the POC fraction in the sediments. Another reason for a too high POC fraction in shallow-water sediments could be the missing of riverine input of lithogenic material. Rivers deliver several petagrams of suspended sediments to the ocean each year (Peucker-Ehrenbrink, 2009; Milliman and Meade, 1983). Most of these particles are deposited close to the continental margins. Such localized effects are not considered here but might need to be investigated in future studies.
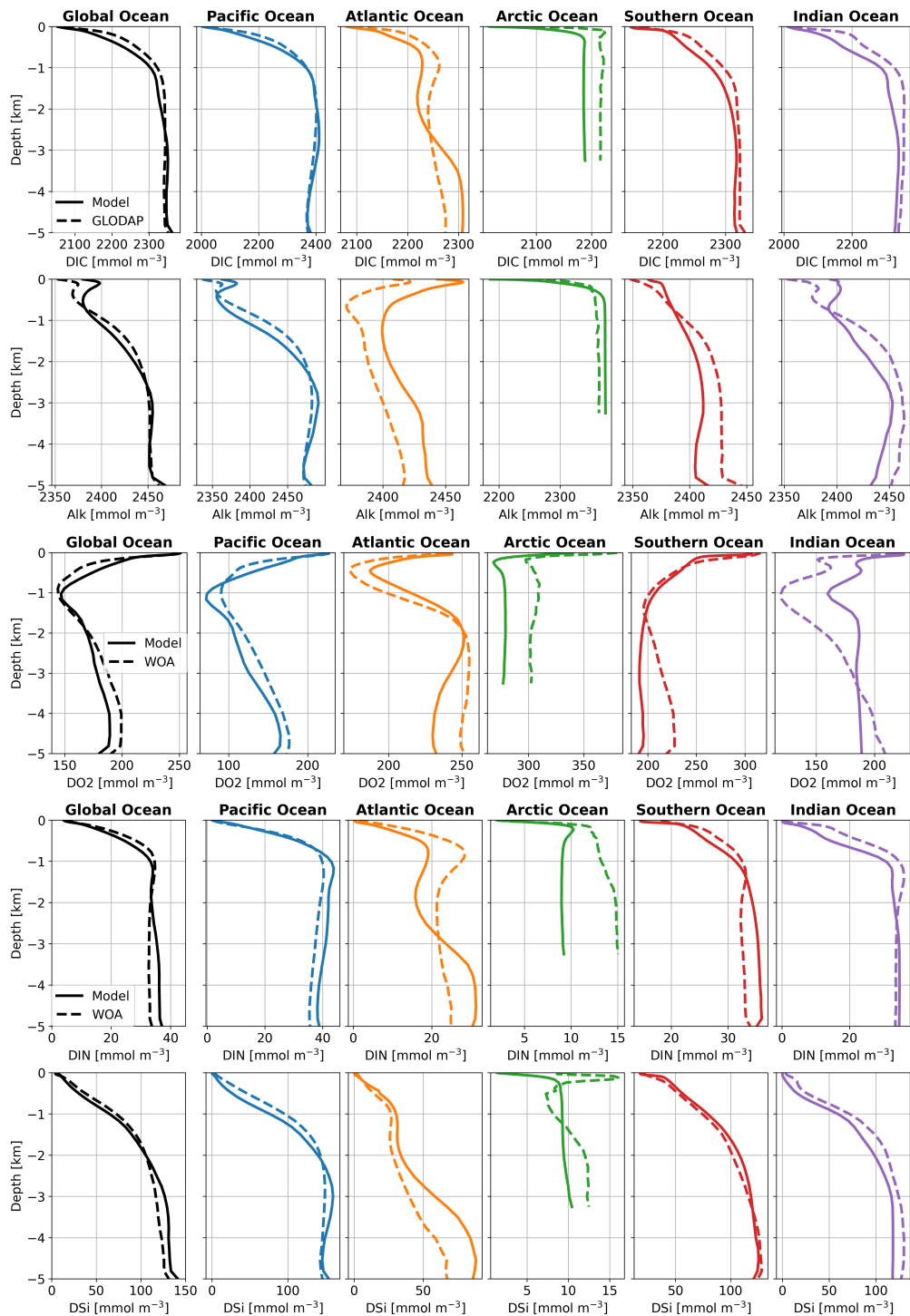
Figure 3. Averaged vertical profiles of DIC, Alk, O_2, DIN and DSi in ocean basins $(\mathrm{mmol\,m^{-3}})$ in R_{spinup}, compared with GLODAPv2 (Large and Yeager, 2009) and WOA data (Garcia et al., 2019) which were used as initial conditions in simulations in this study.
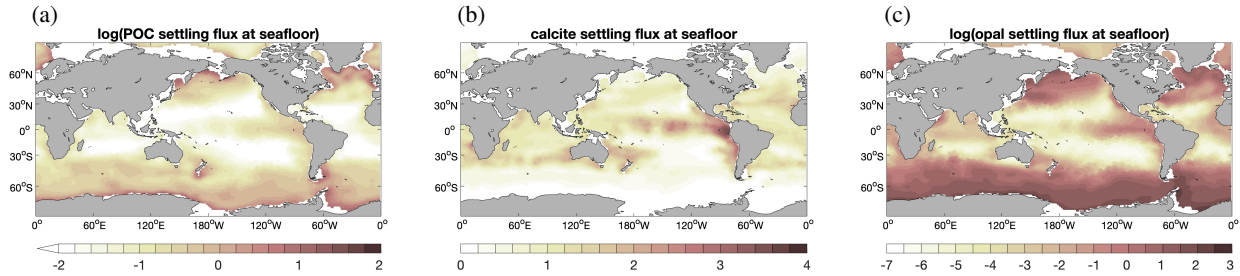
Figure 4. Seafloor deposition rates of (a) POC $(\mathrm{mmol\,C\,m^{-2}\,day^{-1}}$, i.e., the same units as in Dunne et al. (2007)), (b) calcite $(\mathrm{gC\,cm^{-2}\,kyr^{-1}})$ and (c) opal $(\mathrm{gSi\,cm^{-2}\,kyr^{-1}})$ at seafloor in $\mathrm{R_{sedbox}}$.
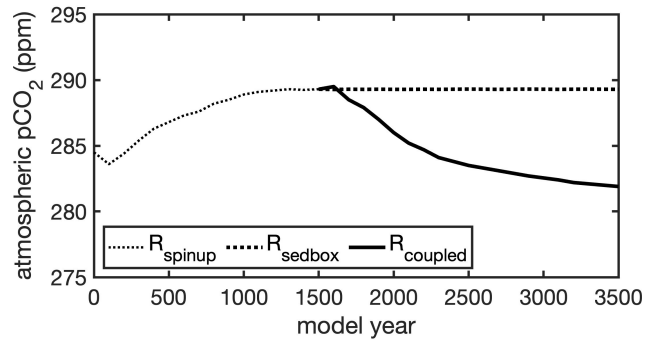
Figure 5. Simulated atmospheric CO$_2$ during 3500 model years: a FESOM2-REcoM3p spinup simulation with an integrated one-layer sediment ($\mathrm{R_{spinup}}$) was run for 1500 years; after 1500 years the model with an integrated one-layer sediment was run for further 2000 years ($\mathrm{R_{sedbox}}$) and a simulation coupled with MEDUSA2 ($\mathrm{R_{coupled}}$) was branched off and run for 2000 years.
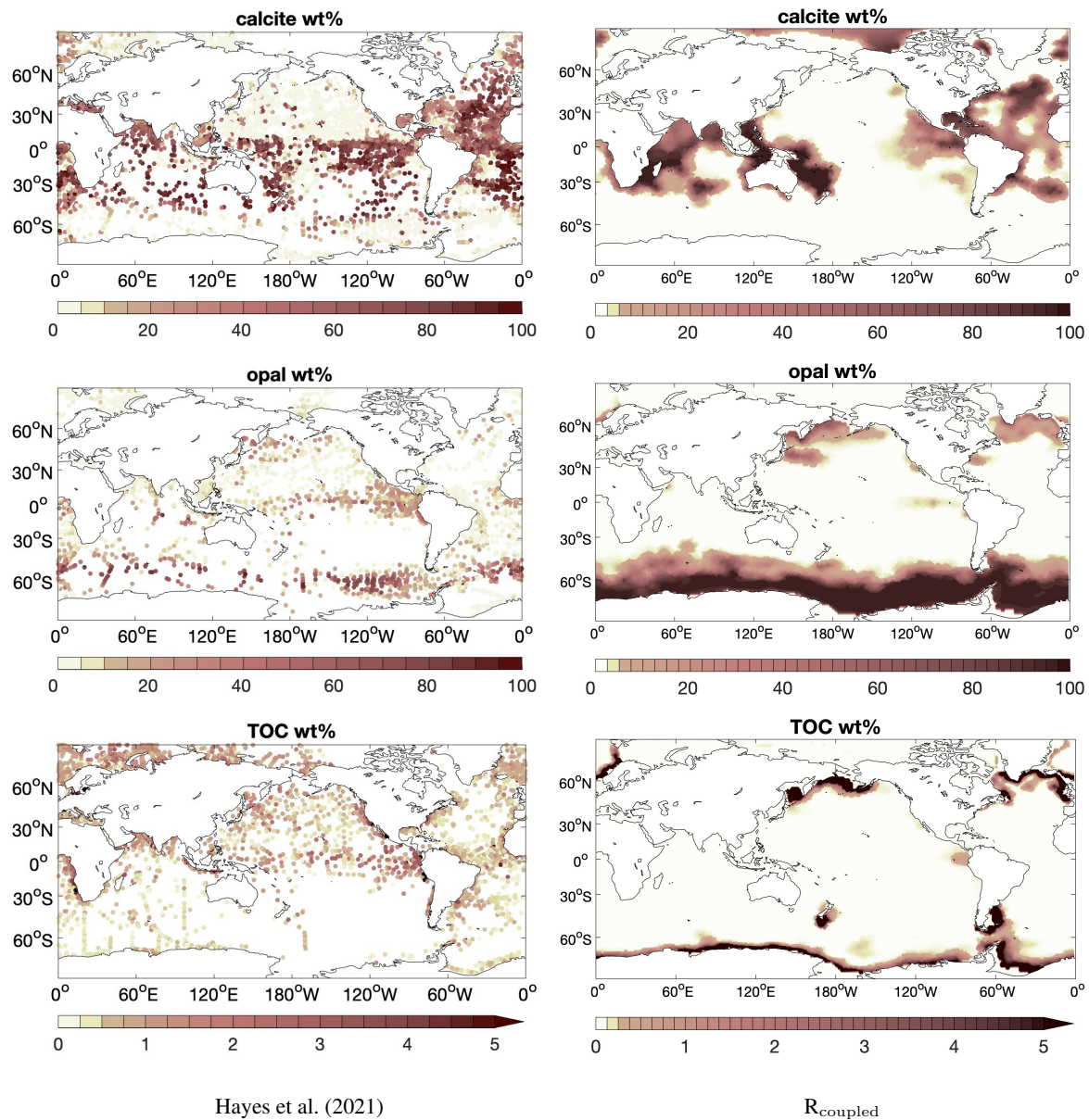
Figure 6. Distribution (weight %) of (row 1) calcite, (row 2) opal and (row 3) total particulate organic carbon (TOC) in the sediment. Left: data compilation by Hayes et al. (2021); Right: results from simulation $R_{coupled}$.

3.2.2 Degradation of organic matter in sediments

375 Two different pathways of degradation of organic matter in sediments are considered here: oxic degradation and denitrification. This setup offers the possibility to have a closer look at their roles in different ocean regions. Figure 7 (left) shows the fraction of oxic degradation in the total degradation. In large areas of the deep-sea sediments, oxic degradation dominates (up to 100%),

whereas denitrification mainly takes place in shallow-water sediments, which results in very low concentrations of NO_3^- in pore waters at high latitudes and in some regions with high biological productivity and thus large input of organic matter.

380   NO_3^- concentrations in these regions are far below its half saturation concentration (Fig. 7 right), potentially leading to an overestimation of the preservation of organic matter in our simulation since no further oxidative degradation is considered in our setup when NO_3^- is exhausted.

The globally integrated denitrification rate of $23\,\mathrm{TgN\,yr^{-1}}$ is within the range of previous estimates of 12–$168\,\mathrm{TgN\,yr^{-1}}$ (DeVries et al., 2013; Thullner et al., 2009; Liu and Kaplan, 1984; Hattori, 1983; Jørgensen, 1983; Codispoti and Christensen,

385   1985; Christensen, 1994; Christensen et al., 1987) albeit at the lower end and much lower than the range of 230–$285\,\mathrm{TgN\,yr^{-1}}$ of Middelburg et al. (1996).

About $39\,\mathrm{TmolC\,yr^{-1}}$ are degraded by aerobic respiration in $R_{coupled}$, which falls in the range of estimates based on oxygen consumption (33–$97\,\mathrm{TmolC\,yr^{-1}}$) for deep-sea sediments (Jahnke, 1996; Christensen, 2000; Andersson et al., 2004; Seiter et al., 2005; Glud, 2008; Jørgensen et al., 2022), but is much lower than estimates of oxygen consumption for the global

390   sediments (99–$212\,\mathrm{TmolC\,yr^{-1}}$, see Snelgrove et al., 2018; Stratmann et al., 2019; Jørgensen et al., 2022).
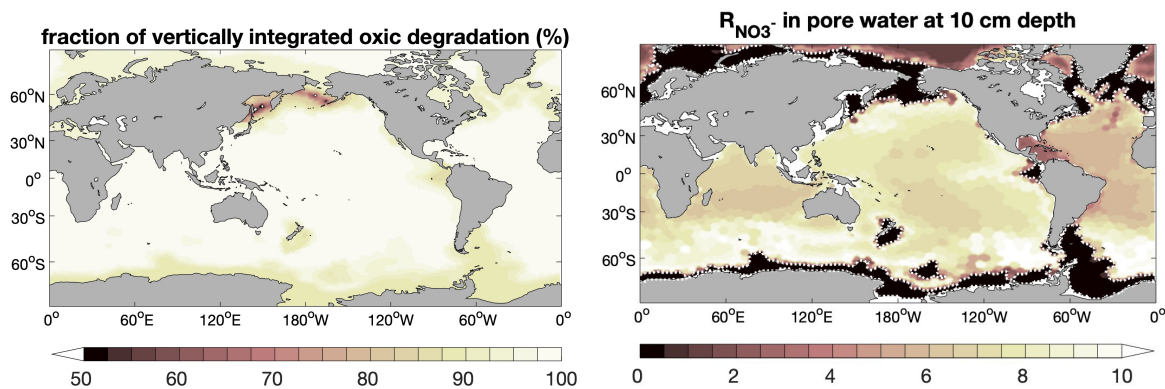
Figure 7. Fraction (%) of vertically integrated organic matter degradation by O_2 in total degradation (left) and the ratio of NO_3^- ($R^{NO_3^-}$) concentration in pore water at the bottom of the bioturbated sedimentary mixed-layer ($10\,\mathrm{cm}$ below the sediment-water interface) to its half saturation concentration ($5\,\mathrm{mmol\,m^{-3}}$ – parameters C_{hnr1} and C_{hnr2} in Table D2). The dotted line in the right-hand panel indicates where the NO_3^- concentration is equal to its half saturation concentration.

3.2.3 Solute exchange across the sediment-water interface

The diffusive flux of DIC from the sediment to the ocean shows a similar pattern to DIN, with high fluxes in regions with high input of organic matter into sediments (Fig. 8a and c). One exception for DIN is the net flux of DIN from the ocean into the sediment along the coasts in the North Pacific. In Fig. 7 these regions are characterised by a high fraction of denitrification in the total degradation, which results in a substantial reduction of DIN in the pore water and thus a net diffusion of DIN from the ocean bottom water to the sediment.

Diffusive fluxes of O_2 show more or less the opposite pattern to DIC. In regions where the seafloor deposition rate of organic matter is high (Fig. 8d), e.g., in the Northern Hemisphere around 60° or in the Southern Ocean, degradation of organic matter leads to a high O_2 flux from the ocean to the sediments as well as high DIC flux from the sediment to the ocean. In the large areas at lower latitudes on the other hand, the DIC and O_2 flux distributions are uncoupled. Here, it is rather the Alk flux (Fig. 8b) that the DIC flux is correlated to.

The Alk flux distribution (Fig. 8b) looks more complex and is the result of two processes that have opposite effects: degradation of organic matter decreases the alkalinity in pore water, while calcite dissolution increases it. Therefore, in those regions where the organic matter degradation rate in the surface sediment is high (i.e., where O_2 uptake is high – Fig. 8d) alkalinity in pore waters may get lowered to the extent that there is a net influx of alkalinity from the ocean bottom water to the sediment. In the Atlantic, the Indian Ocean and parts of the Pacific Ocean where calcite inputs to the sediment are high, alkalinity in pore water is clearly increased and there is a net diffusive flux of alkalinity out of the sediment, into the ocean bottom water. The effect of calcite dissolution is also reflected in the DIC diffusive flux at low to mid-latitudes which is, however, less pronounced in Fig. 8a than in Fig. 8b due to different color scales.
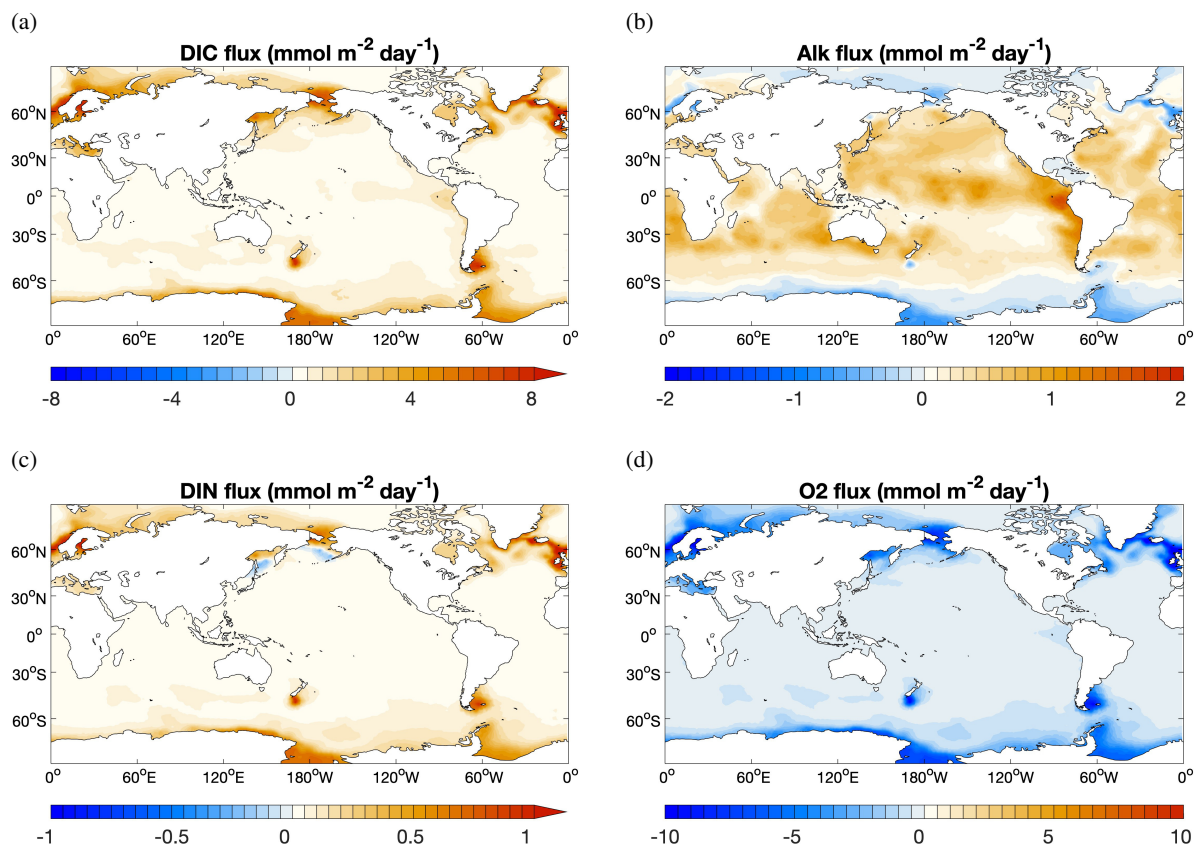
Figure 8. Diffusive flux of DIC, Alk, DIN and O_2 from sediment to ocean $(\mathrm{mol\,m^{-2}\,day^{-1}})$. Sources for the ocean are shown as positive values.

3.2.4 Burial fluxes out of the reactive layer

The simulated POC burial flux in the global sediment ($110\,\mathrm{PgC\,kyr^{-1}}$) is lower than the observed range (160–$2600\,\mathrm{PgC\,kyr^{-1}}$, Tab. 1), consistent with the comparison for the productivity and sinking fluxes. In the deep-sea sediments the simulated flux ($50\,\mathrm{PgC\,kyr^{-1}}$) is within but close to the lower end of the observed range (2–$300\,\mathrm{PgC\,kyr^{-1}}$), reflecting again the inability of our model to represent shallow-water processes with the current resolution.

Similarly, the simulated global burial flux of $CaCO_3$ ($86\,\mathrm{PgC\,kyr^{-1}}$) is much lower than the observation-based estimate ($280\,\mathrm{PgC\,kyr^{-1}}$), while the deep-sea burial of $82\,\mathrm{PgC\,kyr^{-1}}$ is close to the lower end of the observed range of 100–$150\,\mathrm{PgC\,kyr^{-1}}$. The observation-based estimates suggest a roughly equal distribution between shallow and deep-sea environments, while the model simulates only about 5% of the global calcite burial in sediments at depths shallower than $1\,\mathrm{km}$. The possible causes are the omission of some $CaCO_3$ producers in REcoM3p and the coarse resolution which have been already discussed in Sect. 3.1.

The simulated opal burial in deep-sea sediments ($9.5\,\mathrm{Pmol\,Si\,kyr^{-1}}$) slightly exceeds the observed range (5.9–$9.2\,\mathrm{Pmol\,Si\,kyr^{-1}}$), while the global burial of $12\,\mathrm{Pmol\,Si\,kyr^{-1}}$ is clearly higher than the only available estimate of $7.1\,\mathrm{Pmol\,Si\,kyr^{-1}}$ by Tréguer et al. (1995). This study also reported the lowest value of the deep-sea burial.

3.2.5 Impact of the complex sediment on productivity and nutrient supply

The globally averaged vertical distributions of DIC, Alk, O_2 and nutrients do not differ much between R_{sedbox} and $R_{coupled}$ (Fig. B1). O_2 in the Arctic Ocean is largely improved in $R_{coupled}$. In MEDUSA2 O_2 consumption by degradation of organic matter is calculated in dependence of O_2 concentration in sediments, while using the one-layer sediment model, O_2 consumption in sediments is calculated with a fixed O_2:C ratio and subtracted from the bottom water O_2 concentration, likely leading to an overestimation of degradation of organic matter and the lowering of O_2 concentrations in the bottom water. This also applies to other regions with high deposition of organic matter such as the Southern Ocean and parts of the Atlantic Ocean which also show small improvements in the O_2 profiles.

The marine NPP in the coupled simulation $R_{coupled}$ is nearly the same as in R_{sedbox}: it only slightly increases from 35 to $36\,\mathrm{PgC\,yr^{-1}}$. The spatial distribution of the NPP differences between the coupled simulation and R_{sedbox} (Fig. 9) reveals higher productivity by both diatoms and small phytoplankton in coastal regions with large riverine nutrient inputs (DIN and DSi, Fig. 10c and d), which were not considered for R_{sedbox}.

Nutrient supply in the simulations using MEDUSA2 or the one-layer sediment differs in two ways. First, the total diagenetic flux of nutrients from the sediment to the ocean is lower when using MEDUSA2 (Fig. 10a and b; Table 2), since particles sinking into sediment can be stored there: a part is degraded and dissolved in the reactive layer and comes back to bottom water by diffusion, while the rest is buried in the deeper sediments (Munhoven, 2021). This storage and burial delay nutrient recycling and reduce the sedimentary nutrient source when compared to the full degradation and dissolution which takes places in the single-layer sediment. Second, the current riverine source of nutrients considered in the coupled simulation is estimated from the solid burial flux that leaves the reactive sediment layer to be transferred to the core layer in MEDUSA2. This additional
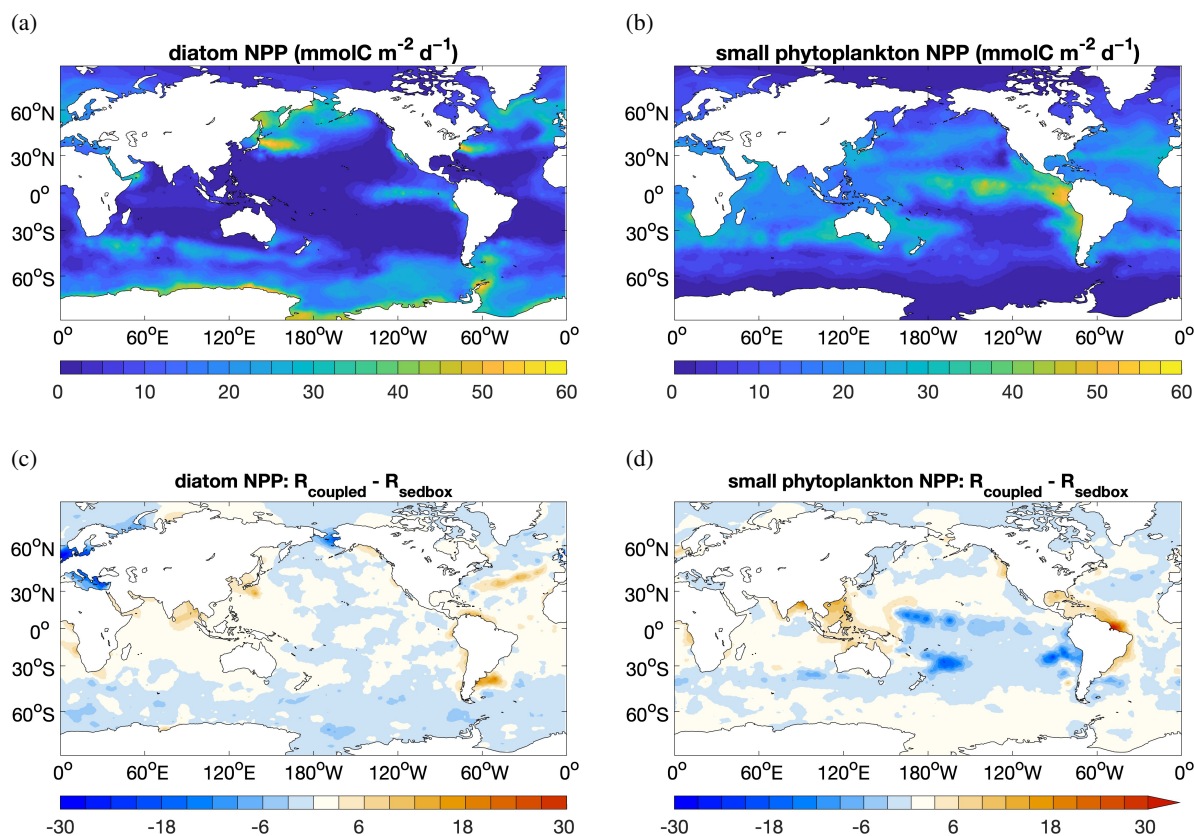
Figure 9. NPP ($\mathrm{mmolC\,m^{-2}\,day^{-1}}$) of (a) diatoms, and (b) small phytoplankton in $\mathrm{R_{sedbox}}$ and the difference in NPP (c, d) between the two simulations ($\mathrm{R_{coupled}}$-minus-$\mathrm{R_{sedbox}}$).

source brings nutrients directly into surface waters near river mouths (Fig. 10c and d). As a result, diatom productivity shows a clear decrease in the North Sea and the Bering Sea (Fig. 9c) where DIN, DSi and DFe from sediments are all significantly
445   reduced (Fig. 10a and b) and no riverine input can cover the loss (Fig. 10c and d).

In $\mathrm{R_{coupled}}$, $12.1\,\mathrm{Tmol\,Si\,year^{-1}}$ are delivered by rivers, while the sedimentary source only decreases from $73.2\,\mathrm{Tmol\,Si\,year^{-1}}$ in $\mathrm{R_{sedbox}}$ to $65.9\,\mathrm{Tmol\,Si\,year^{-1}}$ (Table 2). On the other hand, the riverine input of $1.2\,\mathrm{Tmol\,N\,yr^{-1}}$ cannot compensate the decline in the sediment input from 8.1 to $6.0\,\mathrm{Tmol\,N\,yr^{-1}}$. The nutrients supplied by rivers are, however, directly available for phytoplankton living in surface waters and can still induce phytoplankton growth in areas adjacent to river mouths (Fig. 9c and
450   d), particularly in regions where sedimentary input does not change much (e.g. tropical and subtropical regions). The sedimentary source of iron strongly decreases as well (Table 2), however, the intensity of iron limitation for phytoplankton does not change significantly, since the riverine source is much higher and covers most of the regions where sedimentary input becomes smaller in $\mathrm{R_{coupled}}$.
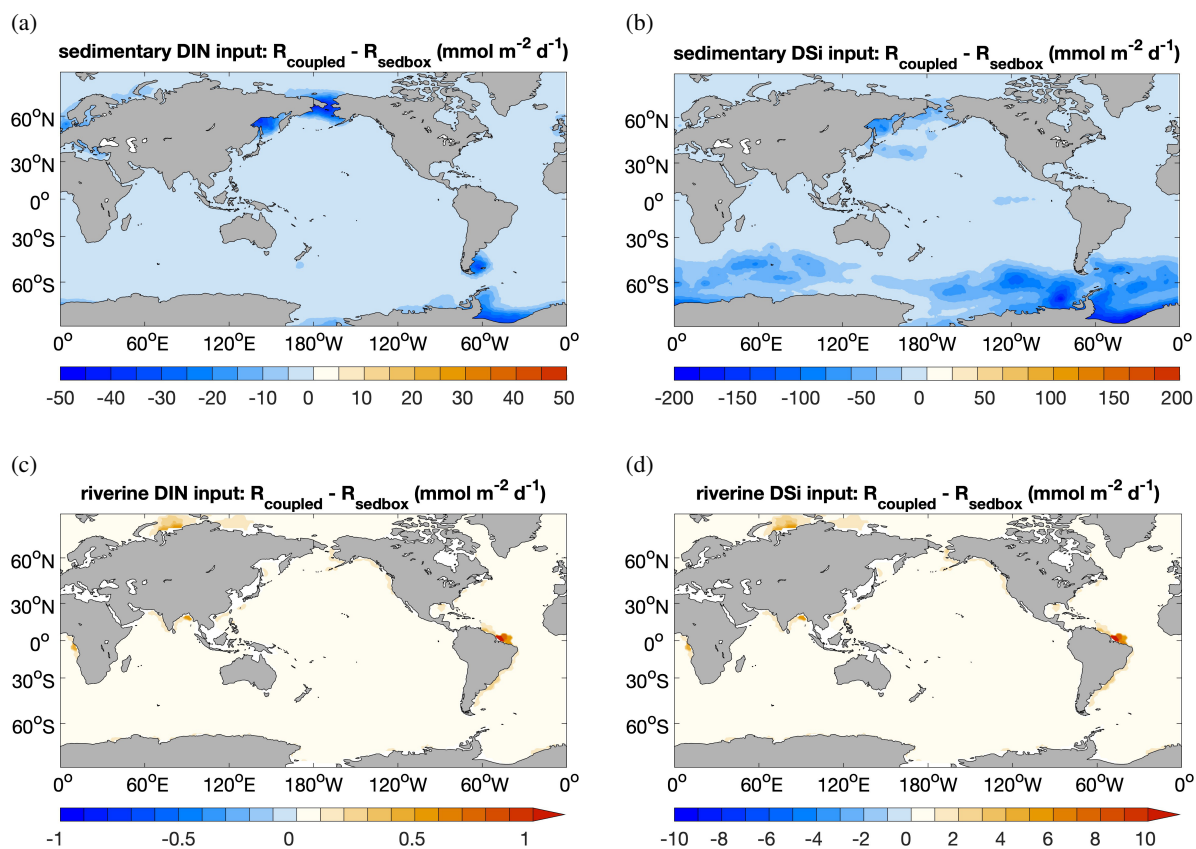
Figure 10. Decrease of sedimentary input of (a) DIN and (b) DSi in $R_{coupled}$ compared to R_{sedbox}; additional riverine input of (c) DIN and (d) DSi in coupled simulations $R_{coupled}$ (mmol m^{-2} day^{-1}). Change in sedimentary input of DFe has an identical spatial pattern as DIN since the iron source is calculated based on DIN source with a constant Fe:N ratio.

Table 2. Fluxes averaged over the last 50 years of the simulations. Positive fluxes are into the ocean or into sediments. Continued on next page. Note that the units here are $\mathrm{Tmol\,yr^{-1}}$, not $\mathrm{Pg\,yr^{-1}}$.

	Ocean balance	$\mathrm{R_{sedbox}}$	$\mathrm{R_{coupled}}$
	riverine input	0	+9.1
	diffusive flux out of sediment	+85.8	+64.5
	seafloor deposition (POC)	−54.2	−48.4
C	seafloor deposition (Calc)	−31.5	−31.6
	air-sea gas exchange	−0.2	+1.5
(Tmol year^{-1})	Sediment balance		
	seafloor deposition (POC)	+54.2	+48.4
	seafloor deposition (Calc)	+31.5	+31.6
	diffusive flux out of sediment	−85.8	−64.5
	burial (POC)	0	−8.9
	burial (Calc)	0	−7.1
	Ocean balance		
	riverine input	0	+11.0
	diffusive flux out of sediment	+47.9	+45.0
Alk	seafloor deposition (PON)	+9.0	+8.0
	seafloor deposition (Calc)	−62.9	−63.3
(Tmol year^{-1})	Sediment balance		
	seafloor deposition (PON)	−9.0	−8.0
	seafloor deposition (Calc)	+62.9	+63.3
	diffusive flux out of sediment	−47.9	−45.0
	burial (POM)	0	+1.2
	burial (Calc)	0	−14.3

	Ocean balance	R_{sedbox}	$R_{coupled}$
	riverine input	0	+1.2
	diffusive NO_3 flux out of sediment	+8.1	+6.0
N	seafloor deposition	−8.0	−7.1
	Sediment balance		
(Tmol year^{-1})	seafloor deposition	+8.0	+7.1
	diffusive NO_3 flux out of sediment	−8.1	−6.0
	burial (PON)	0	−1.2
	Ocean balance		
	riverine input	0	+12.1
Si	diffusive flux out of sediment	+73.2	+65.9
	seafloor deposition	−72.4	−77.7
(Tmol year^{-1})	Sediment balance		
	seafloor deposition	+72.4	+77.7
	diffusive flux out of sediment	−73.2	−65.9
	burial (opal)	0	−12.1
Fe	dust	+5.8	+5.8
(Gmol year^{-1})	rivers	+5.2	+5.2
	diffusive flux out of sediment	+1.2	+0.7

3.2.6 Impact of the complex sediment representation on atmospheric CO_2 and carbon storage

The oceanic carbon pools evolved towards equilibrium concentrations during $R_{coupled}$ by adjusting the gas exchange and the fluxes between ocean and sediment. The atmospheric CO_2 in $R_{coupled}$ declined to 282 ppm after 2000 years which is just slightly below the pre-industrial CO_2 value of 284.3 ppm used initially in R_{spinup}. The air-sea gas exchange is not completely balanced at the end of the run with a net positive CO_2 flux from the atmosphere to the ocean of $1.5 \, \mathrm{TmolC \, yr^{-1}}$ (Table 2), indicating that the atmosphere-ocean-sediment system has not yet reached its equilibrium. This can be seen in the temporal development of CO_2 (Fig. 5) and change in fluxes into and out of the sediment over time (Fig. C1).

We quantified the size of the carbon storage in the reactive sediment layer at the end of $R_{coupled}$, being aware of that the system is still in a transient state. Compared to R_{sedbox}, the ocean contains about 90 Pg more DIC and about 550 PgC is accumulated in the sediment surface layer in $R_{coupled}$, mainly as calcite but with a 12% contribution from POC (Table 3). Emerson and Hedges (1988) estimated a POC storage of 150 PgC in the mixed layer of sediments, while Archer (1996) reported that 800 PgC is stored as calcium carbonate within the 10 cm thick bioturbated layer. Our simulated carbon storage in the surface sediment (70 PgC as POC and 480 PgC as calcite) is lower than these observation-based estimates. One major cause is the underestimation of shallow-water sediments in the coarse-resolution simulation. In R_{sedbox}, POC and calcite are almost completely degraded and dissolved in the single-layer sediment and thus the reservoir sizes of carbon in the sediment are close to zero.

The lowering of atmospheric CO_2 is mainly explained by the long-term storage of material in the sediments combined with the riverine input of alkalinity, which subsequently determines how DIC is distributed into its three species CO_2, HCO_3^-, and CO_3^{2-}, from which only CO_2 can exchange with the atmosphere (Zeebe and Wolf-Gladrow, 2001).

Table 3. Carbon stocks (PgC) in the ocean-sediment system in our two simulations, averaged over the last 50 years.

Reservoir	R_{sedbox}	$R_{coupled}$	Data
DIC	35571	35662	37100[a]
DOC	650	650	662[b]
POC	2	2	3[a]
Sediment POC	< 1	70	150[c]
Sediment calcite	< 1	480	800[d]
Sediment total	< 1	550	

[a] Ciais et al. (2013), pre-industrial estimate
[b] Hansell et al. (2009)
[c] Emerson and Hedges (1988)
[d] Archer (1996)

4 Conclusions

This paper documented the coupling of the sediment model MEDUSA2 to the marine biogeochemical model FESOM2.1-REcoM3p. The coupling was realized via file exchange, the size of the annual fluxes that exchange material between the bottom of the ocean and the sedimentary surface, was updated every 50 years. Results from a coupled simulation in a coarse resolution were presented, while a simulation with a much simpler one-layer sediment was used as reference for comparisons.

The simulation with the coupled model reasonably well reproduced the distribution of DIC, Alk, O_2 and nutrients found in observational data products. Biological productivity, deposition rates of particles onto sediments and the related degradation rates and burial fluxes are underestimated in shallow-water regions (shallower than $1000\,\mathrm{m}$) due to the low model resolution used in this study for technical model developments. Simulated quantities in the deep-sea regions (below 1 km water depth) are within or close to the observed ranges.

While the sediment content of calcite generally agrees well with measurements, the coarse resolution and some missing processes in the ecosystem model lead to some mismatches between simulated and observed sediment content of POC and opal. Nutrient supply from sediments is lower in the coupled simulation than in the simulation with the one-layer sediment, particularly for nitrogen. However, the biological pump is not significantly affected by this decrease, since it is compensated by the additional riverine input of nutrients directly into the surface ocean. Changes in these two sources of nutrients lead to small changes in distribution patterns of diatoms and small phytoplankton. A shift of carbon from the atmosphere to the ocean and sediment reservoir has been found to explain a decrease in atmospheric CO_2 by $\sim 6\,\mathrm{ppm}$ between simulations with and without the complex sediment model. While most of the conclusions here are robust, one should be aware that the exact changes in the carbon reservoirs and in the rates of deposition and burial presented in this paper are results from a transient state of the simulation, as a period of 2000 years is too short for the atmosphere-ocean-sediment system to reach the equilibrium.

Our model setup which includes MEDUSA2 is being further developed for parallel processing. With that, FESOM2.1-REcoM3p-MEDUSA2 can be run in higher spatial resolution for a better representation of shelf regions. Additionally, a version which includes carbon isotopes is under development. Furthermore, REcoM3p-MEDUSA2 will be used as part of the Earth System Model AWI-ESM2 (Shi et al., 2023) to explore changes in the carbon cycle during the last glacial cycle and feedbacks in the Earth's climate system.

Code and data availability. The source code is available at https://doi.org/10.5281/zenodo.8315239.

Author contributions. YY and CV performed the model setup with help from GM, MB and ÖG. YY conducted the simulations and prepared the manuscript with contributions from all co-authors.

Competing interests. No competing interests are present.

Acknowledgements. We thank two anonymous reviewers and the editor for their very constructive comments, which helped to improve the manuscript a lot. YY, PK, CV and MB are supported by the German Federal Ministry of Education and Research (BMBF), as Research for Sustainability initiative (FONA); www.fona.de through the PalMod project (grant number: 01LP1919A). Y.Y is additionally supported by the German Research Foundation (DFG) project (grant number: YE 170/2-1). M.B. is additionally funded through DFG-ANR project MARCARA. Financial support for GM's work on MEDUSA was provided by the Belgian Fund for Scientific Research – F.R.S.-FNRS (project SERENATA, grant no. CDR J.0123.19). GM is a Research Associate with the Belgian Fund for Scientific Research – F.R.S.-FNRS. JH and ÖG were funded by the Initiative and Networking Fund of the Helmholtz Association (Helmholtz Young Investigator Group Marine Carbon and Ecosystem Feedbacks in the Earth System [MarESys], grant number VH-NG-1301).

References

Albani, S., Mahowald, N. M., Perry, A. T., Scanza, R. A., Zender, C. S., Heavens, N. G., Maggi, V., Kok, J. F., and Otto-Bliesner, B. L.: Improved Dust Representation in the Community Atmosphere Model, Journal of Advances in Modeling Earth Systems, 6, 541–570, https://doi.org/10.1002/2013MS000279, 2014.

Amon, R. and Benner, R.: Rapid cycling of high-molecular-weight dissolved organic matter in the ocean, Nature, 369, 549–552, https://doi.org/10.1038/369549a0, 1994.

Andersson, J. H., Wijsman, J. W. M., Herman, P. M. J., Middelburg, J. J., Soetaert, K., and Heip, C.: Respiration patterns in the deep ocean, Geophysical Research Letters, 31, L03 304, https://doi.org/10.1029/2003GL018756, 2004.

Archer, D., Kheshgi, H., and Maier-Reimer, E.: Multiple timescales for neutralization of fossil fuel CO_2, Geophysical Research Letters, 24, 405–408, https://doi.org/10.1029/97GL00168, 1997.

Archer, D., Eby, M., Brovkin, V., Ridgwell, A., Cao, L., Mikolajewicz, U., Caldeira, K., Matsumoto, K., Munhoven, G., Montenegro, A., and Tokos, K.: Atmospheric Lifetime of Fossil Fuel Carbon Dioxide, Annual Review of Earth and Planetary Sciences, 37, 117–134, https://doi.org/10.1146/annurev.earth.031208.100206, 2009.

Archer, D. E.: An atlas of the distribution of calcium carbonate in sediments of the deep sea, Global Biogeochemical Cycles, 10, 159–174, https://doi.org/10.1029/95GB03016, 1996.

Aumont, O., Ethé, C., Tagliabue, A., Bopp, L., and Gehlen, M.: PISCES-v2: An Ocean Biogeochemical Model for Carbon and Ecosystem Studies, Geoscientific Model Development, 8, 2465–2513, https://doi.org/10.5194/gmd-8-2465-2015, 2015.

Börker, J., Hartmann, J., Amann, T., Romero-Mujalli, G., Moosdorf, N., and Jenkins, C.: Chemical Weathering of Loess and Its Contribution to Global Alkalinity Fluxes to the Coastal Zone During the Last Glacial Maximum, Mid-Holocene, and Present, Geochemistry, Geophysics, Geosystems, 21, e2020GC008922, https://doi.org/10.1029/2020GC008922, 2020.

Broecker, W. S. and Peng, T.-H.: The role of $CaCO_3$ compensation in the glacial to interglacial atmospheric CO_2 change, Global Biogeochemical Cycles, 1, 15–29, 1987.

Brovkin, V., Ganopolski, A., Archer, D., and Munhoven, G.: Glacial CO_2 cycle as a succession of key physical and biogeochemical processes, Climate of the Past, 8, 251–264, https://doi.org/10.5194/cp-8-251-2012, 2012.

Buitenhuis, E. T., Le Quéré, C., Bednaršek, N., and Schiebel, R.: Large Contribution of Pteropods to Shallow CaCO3 Export, Global Biogeochemical Cycles, 33, 458–468, https://doi.org/10.1029/2018GB006110, 2019.

Burdige, D. J.: Preservation of Organic Matter in Marine Sediments: Controls, Mechanisms, and an Imbalance in Sediment Organic Carbon Budgets?, Chemical Reviews, 107, 467–485, https://doi.org/10.1021/cr050347q, 2007.

Butzin, M., Ye, Y., Völker, C., Gürses, O., Hauck, J., and Köhler, P.: Carbon isotopes in the marine biogeochemistry model FESOM2.1-REcoM3, EGUsphere, 2023, 1–36, https://doi.org/10.5194/egusphere-2023-1718, 2023.

Cartapanis, O., Bianchi, D., Jaccard, S. L., and Galbraith, E. D.: Global pulses of organic carbon burial in deep-sea sediments during glacial maxima, Nature Communications, 7, https://doi.org/10.5194/gmd-2023-68, 2016.

Cartapanis, O., Galbraith, E. D., Bianchi, D., and Jaccard, S. L.: Carbon Burial in Deep-Sea Sediment and Implications for Oceanic Inventories of Carbon and Alkalinity over the Last Glacial Cycle, Clim. Past, 14, 1819–1850, https://doi.org/10.5194/cp-14-1819-2018, 2018.

Christensen, J. P.: Carbon export from continental shelves, denitrification and atmospheric carbon dioxide, Continental Shelf Research, 14, 547–576, 1994.

Christensen, J. P.: A relationship between deep-sea benthic oxygen demand and oceanic primary productivity, Oceanologica Acta, 23, 65–82, https://doi.org/10.1016/S0399-1784(00)00101-8, 2000.

Christensen, J. P., Murray, J. W., Devol, A. H., and Codispoti, L. A.: Denitrification in continental shelf sediments has major impact on the oceanic nitrogen budget, Global Biogeochemical Cycles, 1, 97–116, 1987.

Ciais, P., Sabine, C., Bala, G., Bopp, L., Brovkin, V., Canadell, J., Chhabra, A., DeFries, R., Galloway, J., Heimann, M., Jones, C., Quéré, C. L., Myneni, R. B., Piao, S., and Thornton, P.: Carbon and Other Biogeochemical Cycles, in: Climate Change 2013: The Physical Science Basis. Contribution of Working Group I to the Fifth Assessment Report of the Intergovernmental Panel on Climate Change, edited by Stocker, T. F., Qin, D., Plattner, G.-K., Tignor, M. M. B., Allen, S. K., Boschung, J., Nauels, A., Xia, Y., Bex, V., and Midgley, P. M., chap. 6, pp. 465–570, Cambridge University Press, https://www.ipcc.ch/site/assets/uploads/2018/02/WG1AR5_Chapter06_FINAL.pdf, 2013.

Codispoti, L. and Christensen, J.: Nitrification, denitrification and nitrous oxide cycling in the eastern tropical South Pacific Ocean, Marine chemistry, 16, 277–300, 1985.

de Baar, H. J. W. and de Jong, J.: Distributions, Sources and Sinks of Iron in Seawater, in: The Biogeochemistry of Iron in Seawater, edited by Turner, D. R. and Hunter, K. A., vol. 7 of *IUPAC Ser. Anal. Phys. Chem. Environ. Syst.*, pp. 123–253, John Wiley & Sons, 2001.

DeVries, T., Deutsch, C., Rafter, P. A., and Primeau, F.: Marine denitrification rates determined from a global 3-D inverse model, Biogeosciences, 10, 2481–2496, https://doi.org/10.5194/bg-10-2481-2013, 2013.

Dunne, J. P., Sarmiento, J. L., and Gnanadesikan, A.: A synthesis of global particle export from the surface ocean and cycling through the ocean interior and on the seafloor, Global Biogeochemical Cycles, 21, GB4006, https://doi.org/10.1029/2006GB002907, 2007.

Dunne, J. P., Hales, B., and Toggweiler, J. R.: Global calcite cycling constrained by sediment preservation controls, Global Biogeochemical Cycles, 26, GB3023, https://doi.org/10.1029/2010GB003935, 2012.

Elrod, V. A., Berelson, W. M., Coale, K. H., and Johnson, K. S.: The flux of iron from continental shelf sediments: A missing source for global budgets, Geophysical Research Letters, 31, https://doi.org/10.1029/2004GL020216, 2004.

Emerson, S. and Hedges, J. I.: Processes controlling the organic carbon content of open ocean sediments, Paleoceanography, 3, 621–634, https://doi.org/10.1029/PA003i005p00621, 1988.

Friedlingstein, P., O'Sullivan, M., Jones, M. W., Andrew, R. M., Gregor, L., Hauck, J., Le Quéré, C., Luijkx, I. T., Olsen, A., Peters, G. P., Peters, W., Pongratz, J., Schwingshackl, C., Sitch, S., Canadell, J. G., Ciais, P., Jackson, R. B., Alin, S. R., Alkama, R., Arneth, A., Arora, V. K., Bates, N. R., Becker, M., Bellouin, N., Bittig, H. C., Bopp, L., Chevallier, F., Chini, L. P., Cronin, M., Evans, W., Falk, S., Feely, R. A., Gasser, T., Gehlen, M., Gkritzalis, T., Gloege, L., Grassi, G., Gruber, N., Gürses, Ö., Harris, I., Hefner, M., Houghton, R. A., Hurtt, G. C., Iida, Y., Ilyina, T., Jain, A. K., Jersild, A., Kadono, K., Kato, E., Kennedy, D., Klein Goldewijk, K., Knauer, J., Korsbakken, J. I., Landschützer, P., Lefèvre, N., Lindsay, K., Liu, J., Liu, Z., Marland, G., Mayot, N., McGrath, M. J., Metzl, N., Monacci, N. M., Munro, D. R., Nakaoka, S.-I., Niwa, Y., O'Brien, K., Ono, T., Palmer, P. I., Pan, N., Pierrot, D., Pocock, K., Poulter, B., Resplandy, L., Robertson, E., Rödenbeck, C., Rodriguez, C., Rosan, T. M., Schwinger, J., Séférian, R., Shutler, J. D., Skjelvan, I., Steinhoff, T., Sun, Q., Sutton, A. J., Sweeney, C., Takao, S., Tanhua, T., Tans, P. P., Tian, X., Tian, H., Tilbrook, B., Tsujino, H., Tubiello, F., van der Werf, G. R., Walker, A. P., Wanninkhof, R., Whitehead, C., Willstrand Wranne, A., Wright, R., Yuan, W., Yue, C., Yue, X., Zaehle, S., Zeng, J., and Zheng, B.: Global Carbon Budget 2022, Earth System Science Data, 14, 4811–4900, https://doi.org/10.5194/essd-14-4811-2022, 2022.

Garcia, H. E., Locarnini, R. A., Boyer, T. P., Antonov, J. I., Baranova, O. K., Zweng, M. M., Reagan, J. R., and Johnson, D. R.: World Ocean Atlas 2013, Volume 4: Dissolved Inorganic Nutrients (Phosphate, Nitrate, Silicate). S. Levitus, Ed., A. Mishonov Technical Ed., Tech. rep., NOAA Atlas NESDIS 76, 2014.

585 Garcia, H. E., Weathers, K. W., Paver, C. R., Smolyar, I., Boyer, T. P., Locarnini, R. A., Zweng, M. M., Mishonov, A. V., Baranova, O. K., Seidov, D., and Reagan, J. R.: World Ocean Atlas 2018, Volume 3: Dissolved Oxygen, Apparent Oxygen Utilization, and Oxygen Saturation. A. Mishonov Technical Editor, Tech. rep., NOAA Atlas NESDIS 83, 2019.

Glud, R. N.: Oxygen dynamics of marine sediments, Marine Biology Research, 4, 243–289, https://doi.org/10.1080/17451000801888726, 2008.

590 Guieu, C., Huang, W. W., Martin, J.-M., and Yong, Y. Y.: Outflow of trace metals into the Laptev Sea by the Lena River, Marine Chemistry, 53, 255–267, https://doi.org/10.1016/0304-4203(95)00093-3, 1996.

Gürses, O., Oziel, L., Karakuş, O., Sidorenko, D., Völker, C., Ye, Y., Zeising, M., Butzin, M., and Hauck, J.: Ocean biogeochemistry in the coupled ocean–sea ice–biogeochemistry model FESOM2.1–REcoM3, Geoscientific Model Development, 16, 4883–4936, https://doi.org/10.5194/gmd-16-4883-2023, 2023.

595 Hansell, D. A., Carlson, C. A., Repeta, D. J., and Schlitzer, R.: Dissolved Organic Matter in the Ocean : A Controversy Stimulates New Insights, Oceanography, 22, https://doi.org/10.5670/oceanog.2009.109, 2009.

Hattori, A.: Denitrification and dissimilatory nitrate reduction, in: Nitrogen in the marine environment, edited by Carpenter, E. J. and Capone, D. G., chap. 6, pp. 191–232, Academic Press, New York (NY), 1 edn., 1983.

Hayes, C. T., Costa, K. M., Anderson, R. F., Calvo, E., Chase, Z., Demina, L. L., Dutay, J.-C., German, C. R., Heimbürger-Boavida, L.-E., 600 Jaccard, S. L., Jacobel, A., Kohfeld, K. E., Kravchishina, M. D., Lippold, J., Mekik, F., Missiaen, L., Pavia, F. J., Paytan, A., Pedrosa-Pamies, R., Petrova, M. V., Rahman, S., Robinson, L. F., Roy-Barman, M., Sanchez-Vidal, A., Shiller, A., Tagliabue, A., Tessin, A. C., Van Hulten, M., and Zhang, J.: Global Ocean Sediment Composition and Burial Flux in the Deep Sea, Global Biogeochemical Cycles, 35, e2020GB006769, https://doi.org/10.1029/2020GB006769, 2021.

Heinze, C., Maier-Reimer, E., Winguth, A. M. E., and Archer, D.: A Global Oceanic Sediment Model for Long-Term Climate Studies, Global 605 Biogeochemical Cycles, 13, 221–250, https://doi.org/10.1029/98GB02812, 1999.

Hilton, R. G. and West, A. J.: Mountains, erosion and the carbon cycle, Nature Reviews Earth and Environment, 1, https://doi.org/10.1038/s43017-020-0058-6, 2020.

Himstedt, K.: Multiple Execution of the Same MPI Application to Exploit Parallelism at Hotspots with Minimal Code Changes: A Case Study with FESOM2-Iceberg and FESOM2-REcoM, EGUsphere, 2023, 1–27, https://doi.org/10.5194/egusphere-2023-756, 2023.

610 Hohn, S.: Coupling and decoupling of biogeochemical cycles in marine ecosystems, Ph.D. thesis, Universität Bremen, Fachbereich Biologie, 2009.

Jahnke, R. A.: The global ocean flux of particulate organic carbon: Areal distribution and magnitude, Global Biogeochemical Cycles, 10, 71–88, https://doi.org/10.1029/95GB03525, 1996.

Jørgensen, B. B.: Processes at the sediment-water interface, in: The Major Biogeochemical Cycles and Their Interactions, edited by Bolin, 615 B. and Cook, R. B., vol. 21 of *SCOPE Reports*, pp. 477–509, John Wiley and Sons, New York (NY), 1983.

Jørgensen, B. B., Wenzhöfer, F., Egger, M., and Glud, R. N.: Sediment oxygen consumption: Role in the global marine carbon cycle, Earth-Science Reviews, 228, 103 987, https://doi.org/10.1016/j.earscirev.2022.103987, 2022.

Keppler, L., Landschützer, P., Gruber, N., Lauvset, S. K., and Stemmler, I.: Seasonal Carbon Dynamics in the Near-Global Ocean, Global Biogeochemical Cycles, 34, e2020GB006571, https://doi.org/10.1029/2020GB006571, 2020.

620 Knecht, N. S., Benedetti, F., Hofmann Elizondo, U., Bednaršek, N., Chaabane, S., de Weerd, C., Peijnenburg, K. T. C. A., Schiebel, R., and Vogt, M.: The Impact of Zooplankton Calcifiers on the Marine Carbon Cycle, Global Biogeochemical Cycles, 37, e2022GB007685, https://doi.org/10.1029/2022GB007685, 2023.

Köhler, P.: Anthropogenic CO_2 of high emission scenario compensated after 3500 years of ocean alkalinization with an annually constant dissolution of 5 Pg of olivine, Frontiers in Climate, 2, 575744, https://doi.org/10.3389/fclim.2020.575744, 2020.

625 Köhler, P. and Munhoven, G.: Late Pleistocene carbon cycle revisited by considering solid Earth processes, Paleoceanography and Paleoclimatology, 35, e2020PA004020, https://doi.org/10.1029/2020PA004020, 2020.

Krachler, R., Jirsa, F., and Ayromlou, S.: Factors influencing the dissolved iron input by river water to the open ocean, Biogeosciences, 2, 311–315, https://doi.org/10.5194/bg-2-311-2005, 2005.

Kriest, I. and Oschlies, A.: Swept under the Carpet: Organic Matter Burial Decreases Global Ocean Biogeochemical Model Sensitivity to
630 Remineralization Length Scale, Biogeosciences, 10, 8401–8422, https://doi.org/10.5194/bg-10-8401-2013, 2013.

Kurahashi-Nakamura, T., Paul, A., Munhoven, G., Merkel, U., and Schulz, M.: Coupling of a Sediment Diagenesis Model (MEDUSA) and an Earth System Model (CESM1.2): A Contribution toward Enhanced Marine Biogeochemical Modelling and Long-Term Climate Simulations, Geoscientific Model Development, 13, 825–840, https://doi.org/10.5194/gmd-13-825-2020, 2020.

Lan, X., Tans, P., and K.W., T.: Trends in globally-averaged CO_2 determined from NOAA Global Monitoring Laboratory measurements.
635 Version 2023-06, https://doi.org/10.15138/9N0H-ZH07, 2023.

Large, W. G. and Yeager, S. G.: The Global Climatology of an Interannually Varying Air-Sea Flux Data Set, Climate Dynamics, 33, 341–364, https://doi.org/10.1007/s00382-008-0441-3, 2009.

Lauvset, S. K., Key, R. M., Olsen, A., van Heuven, S., Velo, A., Lin, X., Schirnick, C., Kozyr, A., Tanhua, T., Hoppema, M., Jutterström, S., Steinfeldt, R., Jeansson, E., Ishii, M., Perez, F. F., Suzuki, T., and Watelet, S.: A New Global Interior Ocean Mapped Climatology: The
640 1×1 GLODAP Version 2, Earth System Science Data, 8, 325–340, https://doi.org/10.5194/essd-8-325-2016, 2016.

Liu, K.-K. and Kaplan, I. R.: Denitrification rates and availability of organic matter in marine environments, Earth and Planetary Science Letters, 68, 88–100, 1984.

Martin, J. H., Knauer, G. A., Karl, D. M., and Broenkow, W. W.: VERTEX: carbon cycling in the northeast Pacific, Deep Sea Research Part A. Oceanographic Research Papers, 34, 267–285, https://doi.org/10.1016/0198-0149(87)90086-0, 1987.

645 Meinshausen, M., Smith, S. J., Calvin, K., Daniel, J. S., Kainuma, M. L., Lamarque, J.-F., Matsumoto, K., Montzka, S. A., Raper, S. C., Riahi, K., et al.: The RCP greenhouse gas concentrations and their extensions from 1765 to 2300, Climatic change, 109, 213–241, 2011.

Meinshausen, M., Vogel, E., Nauels, A., Lorbacher, K., Meinshausen, N., Etheridge, D., Fraser, P., Montzka, S. A., Rayner, P., Trudinger, C., Krummel, P., Beyerle, U., Cannadell, J. G., Daniel, J. S., Enting, I., Law, R. M., O'Doherty, S., Prinn, R. G., Reimann, S., Rubino, M., Velders, G. J. M., Vollmer, M. K., and Weiss, R.: Historical greenhouse gas concentrations for climate modelling (CMIP6), Geoscientific
650 Model Development, 10, 2057–2116, https://doi.org/10.5194/gmd-10-2057-2017, 2017.

Middelburg, J. J., Soetaert, K., Herman, P. M. J., and Heip, C. H. R.: Denitrification in marine sediments: A model study, Global Biogeochemical Cycles, 10, 661–673, https://doi.org/10.1029/96GB02562, 1996.

Milliman, J. D. and Meade, R. H.: World-wide delivery of river sediment to the oceans, JGeol, 91, 1–21, https://doi.org/10.1086/628741, 1983.

655 Moreira Martinez, S., Roche, D. M., Munhoven, G., and Waelbroeck, C.: Coupling MEDUSA sediment model to iLOVECLIM (v1.1β) Earth system model, in: 12th International Conference on Paleoceanography (ICP12)., pp. P–368, Utrecht (NL), http://icp12.uu.nl/wp-content/uploads/2016/08/Poster-abstracts-sessie-3.pdf, 2016.

Muller-Karger, F. E., Varela, R., Thunell, R., Luers sen, R., Hu, C., and Walsh, J. J.: The importance of continental margins in the global carbon cycle, Geophysical Research Letters, 32, L01602, https://doi.org/10.1029/2004GL021346, 2005.

660 Munhoven, G.: Glacial–Interglacial Rain Ratio Changes: Implications for Atmospheric and Ocean–Sediment Interaction, Deep Sea Research Part II: Topical Studies in Oceanography, 54, 722–746, https://doi.org/10.1016/j.dsr2.2007.01.008, 2007.

Munhoven, G.: Model of Early Diagenesis in the Upper Sediment with Adaptable Complexity – MEDUSA (v. 2): A Time-Dependent Biogeochemical Sediment Module for Earth System Models, Process Analysis and Teaching, Geoscientific Model Development, 14, 3603–3631, https://doi.org/10.5194/gmd-14-3603-2021, 2021.

665 Nelson, D. M., Tréguer, P., Brzezinski, M. A., Leynaert, A., and Qu'eguiner, B.: Production and dissolution of biogenic silica in the ocean: Revised global estimates, comparison with regional data and relationship to biogenic sedimentation, Global Biogeochemical Cycles, 9, 359–372, https://doi.org/10.1029/95GB01070, 1995.

Peucker-Ehrenbrink, B.: Land2Sea database of river drainage basin sizes, annual water discharges, and suspended sediment fluxes, Geochemistry, Geophysics, Geosystems, 10, https://doi.org/10.1029/2008GC002356, 2009.

670 Picard, A., Davis, R. S., Gläser, M., and Fujii, K.: Revised formula for the density of moist air (CIPM-2007), Metrologia, 45, 149–155, https://doi.org/10.1088/0026-1394/45/2/004, 2008.

Sarmiento, J. L. and Gruber, N.: Ocean Biogeochemical Dynamics, Princeton University Press, https://doi.org/10.2307/j.ctt3fgxqx, 2006.

Sarmiento, J. L., Dunne, J., Gnanadesikan, A., Key, R. M., Matsumoto, K., and Slater, R.: A new estimate of the $CaCO_3$ to organic carbon export ratio, Global Biogeochemical Cycles, 16, 1107, https://doi.org/10.1029/2002GB001919, 2002.

675 Schartau, M., Engel, A., Schröter, J., Thoms, S., Völker, C., and Wolf-Gladrow, D.: Modelling carbon overconsumption and the formation of extracellular particulate organic carbon, Biogeosciences, 4, 433–454, https://doi.org/10.5194/bg-4-433-2007, 2007.

Scholz, P., Sidorenko, D., Gurses, O., Danilov, S., Koldunov, N., Wang, Q., Sein, D., Smolentseva, M., Rakowsky, N., and Jung, T.: Assessment of the Finite-volumE Sea Ice-Ocean Model (FESOM2.0) – Part 1: Description of Selected Key Model Elements and Comparison to Its Predecessor Version, Geoscientific Model Development, 12, 4875–4899, https://doi.org/10.5194/gmd-12-4875-2019, 2019.

680 Scholz, P., Sidorenko, D., Danilov, S., Wang, Q., Koldunov, N., Sein, D., and Jung, T.: Assessment of the Finite-VolumE Sea Ice–Ocean Model (FESOM2.0) – Part 2: Partial Bottom Cells, Embedded Sea Ice and Vertical Mixing Library CVMix, Geoscientific Model Development, 15, 335–363, https://doi.org/10.5194/gmd-15-335-2022, 2022.

Séférian, R., Berthet, S., Yool, A., Palmiéri, J., Bopp, L., Tagliabue, A., Kwiatkowski, L., Aumont, O., Christian, J., Dunne, J., Gehlen, M., Ilyina, T., John, J. G., Li, H., Long, M. C., Luo, J. Y., Nakano, H., Romanou, A., Schwinger, J., Stock, C., Santana-Falcón, Y., Takano, Y.,
685 Tjiputra, J., Tsujino, H., Watanabe, M., Wu, T., Wu, F., and Yamamoto, A.: Tracking Improvement in Simulated Marine Biogeochemistry Between CMIP5 and CMIP6, Current Climate Change Reports, 6, 95–119, https://doi.org/10.1007/s40641-020-00160-0, 2020.

Seifert, M., Nissen, C., Rost, B., and Hauck, J.: Cascading effects augment the direct impact of CO2 on phytoplankton growth in a biogeochemical model, Elementa: Science of the Anthropocene, 10, 00 104, https://doi.org/10.1525/elementa.2021.00104, 2022.

Seiter, K., Hensen, C., Schröter, J., and Zabel, M.: Organic Carbon Content in Surface Sediments — Defining Regional Provinces, Deep Sea
690 Research Part I: Oceanographic Research Papers, 51, 2001–2026, https://doi.org/10.1016/j.dsr.2004.06.014, 2004.

Seiter, K., Hensen, C., and Zabel, M.: Benthic carbon mineralization on a global scale, Global Biogeochemical Cycles, 19, https://doi.org/10.1029/2004GB002225, 2005.

Shi, X., Cauquoin, A., Lohmann, G., Jonkers, L., Wang, Q., Yang, H., Sun, Y., and Werner, M.: Simulated stable water isotopes during the mid-Holocene and pre-industrial using AWI-ESM-2.1-wiso, Geoscientific Model Development Discussions, 2023, 1–39,
695 https://doi.org/10.5194/gmd-2023-68, 2023.

Snelgrove, P. V., Soetaert, K., Solan, M., Thrush, S., Wei, C.-L., Danovaro, R., Fulweiler, R. W., Kitazato, H., Ingole, B., Norkko, A., Parkes, R. J., and Volkenborn, N.: Global Carbon Cycling on a Heterogeneous Seafloor, Trends in Ecology & Evolution, 33, 96–105, https://doi.org/10.1016/j.tree.2017.11.004, 2018.

Steele, M., Morley, R., and Ermold, W.: PHC: A Global Ocean Hydrography with a High-Quality Arctic Ocean, Journal of Climate, 14, 2079–2087, https://doi.org/10.1175/1520-0442(2001)014<2079:PAGOHW>2.0.CO;2, 2001.

Stratmann, T., Wei, C.-L., Lin, Y.-S., and van Oevelen, D.: The SCOC database, a large, open, and global database with sediment community oxygen consumption rates, Scientific Data, 6, https://doi.org/10.1038/s41597-019-0259-3, 2019.

Thullner, M., Dale, A. W., and Regnier, P.: Global-scale quantification of mineralization pathways in marine sediments: A reaction-transport modeling approach, Geochemistry, Geophysics, Geosystems, 10, Q10012, https://doi.org/https://doi.org/10.1029/2009GC002484, 2009.

Tréguer, P., Nelson, D. M., Bennekom, A. J. V., DeMaster, D. J., Leynaert, A., and Quéguiner, B.: The Silica Balance in the World Ocean: A Reestimate, Science, 268, 375–379, https://doi.org/10.1126/science.268.5209.375, 1995.

Tréguer, P. J. and De La Rocha, C. L.: The World Ocean Silica Cycle, Annual Review of Marine Science, 5, 477–501, https://doi.org/10.1146/annurev-marine-121211-172346, 2013.

Tréguer, P. J., Sutton, J. N., Brzezinski, M., Charette, M. A., Devries, T., Dutkiewicz, S., Ehlert, C., Hawkings, J., Leynaert, A., Liu, S. M., Llopis Monferrer, N., López-Acosta, M., Maldonado, M., Rahman, S., Ran, L., and Rouxel, O.: Reviews and Syntheses: The Biogeochemical Cycle of Silicon in the Modern Ocean, Biogeosciences, 18, 1269–1289, https://doi.org/10.5194/bg-18-1269-2021, 2021.

Trenberth, K. E. and Smith, L.: The Mass of the Atmosphere: A Constraint on Global Analyses, Journal of Climate, 18, 864–875, https://doi.org/10.1175/JCLI-3299.1, 2005.

Volk, T. and Hoffert, M. I.: Ocean Carbon Pumps : Analysis of Relative Strengths and Efficiencies in Ocean-Driven Atmospheric CO_2 Changes, in: The Carbon Cycle and Atmospheric CO_2 : Natural Variations Archean to Present, edited by Sundquist, E. T. and Broecker, W. S., vol. 32 of *Geophysical Monograph Series*, pp. 99–110, American Geophysical Union (AGU), Washington (DC), https://doi.org/10.1029/GM032p0099, 1985.

Wanninkhof, R.: Relationship between wind speed and gas exchange over the ocean revisited, Limnology and Oceanography: Methods, 12, 351–362, https://doi.org/10.4319/lom.2014.12.351, 2014.

Zeebe, R. E. and Wolf-Gladrow, D. A.: CO_2 in Seawater: Equilibrium, Kinetics, Isotopes, vol. 65 of *Elsevier Oceanography Book Series*, Elsevier Science Publishing, Amsterdam, The Netherlands, 2001.

Appendix A: Figures
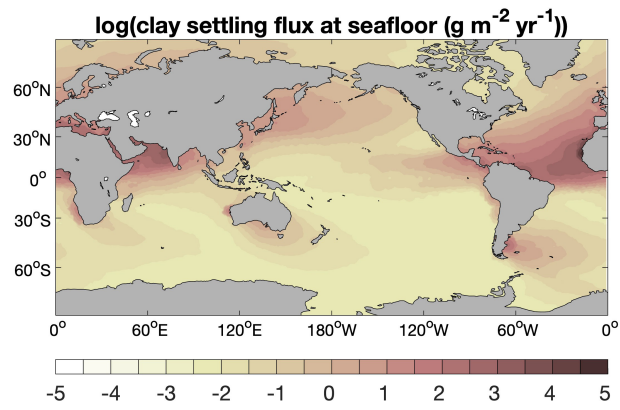
Figure A1. Clay flux at sediment–water interface $(\mathrm{g\,m^{-2}\,yr^{-1}})$.
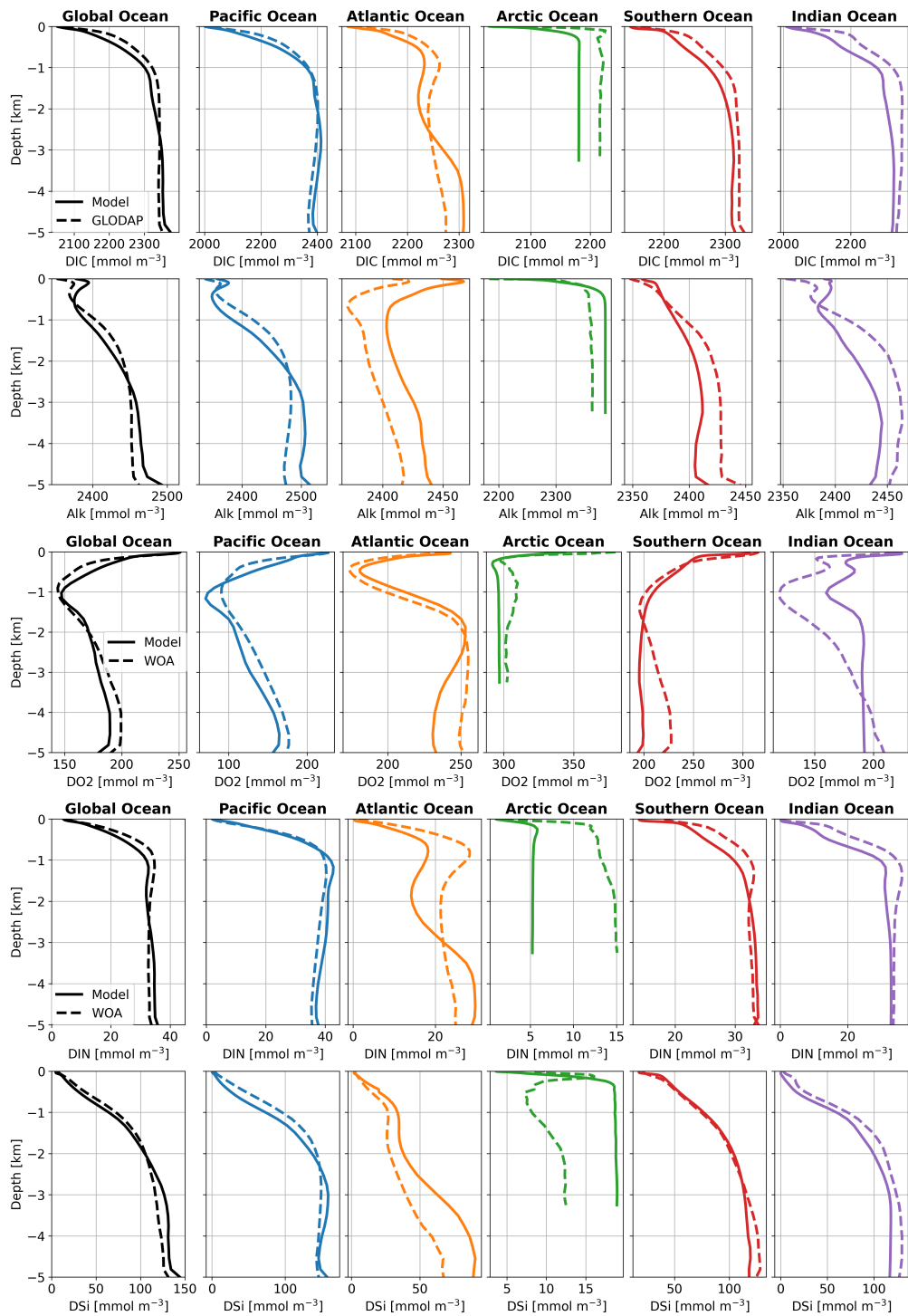
Figure B1. Averaged vertical profiles of DIC, Alk, O_2, DIN and DSi in ocean basins ($\mathrm{mmol\,m^{-3}}$) in $\mathrm{R_{coupled}}$, compared with GLODAP and WOA data which were used as initial conditions in simulations in this study.
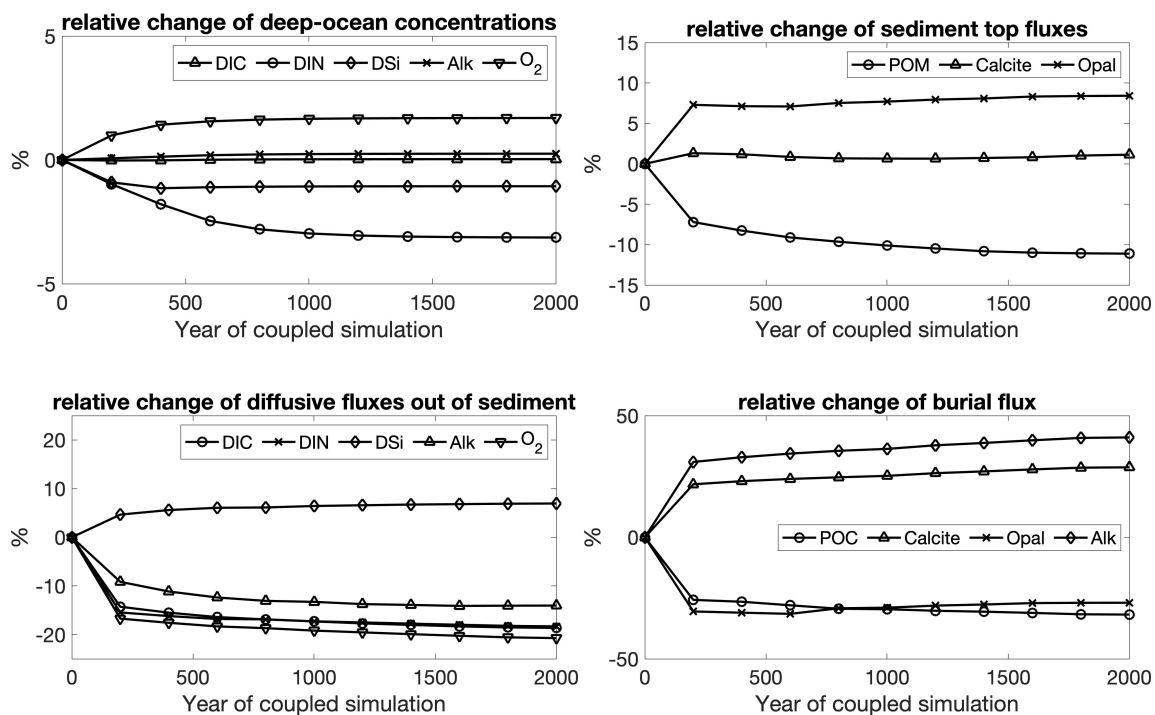
Figure C1. Temporal changes of deep ocean concentrations (DIC, DIN, DSi, Alk and O_2) (upper left), deposition rates of POM, calcite and opal onto sediment top (upper right), diffusive fluxes of solutes out of sediments (lower left) and burial fluxes (lower right) during the 2000-year coupled simulation $R_{coupled}$. Changes are in percentages relative to the values at the beginning of $R_{coupled}$.

Appendix D: Model parameters

D1 FESOM2.1-REcoM3p

Table D1. Parameters in REcoM3 modified in this study compared to Gürses et al. (2023)

Parameter	Value	Description	Unit
$V det_a$	0.036	Slope of depth-dependent sinking velocity of detritus	$[\mathrm{d}^{-1}]$
$V calc$	0.0072	Slope of depth-dependent dissolution rate of calcite	$[\mathrm{d}^{-1}]$

725     $V calc$ replaces 0.0288 in Eq. A29 in Gürses et al. (2023).

D2 MEDUSA2

Table D2. Reaction rate law expressions and parameter values used for the early diagenetic reaction network in MEDUSA2. C_{cs} is the CO_3^{2-} concentration in seawater at saturation with respect to calcite. $(\dots)^+$ denotes the positive part of $(\dots)$. C_{hox1} and C_{hox1} are the half-saturation concentrations of O_2 for the oxic remineralisation of the organic organic matter classes POM_1 and POM_2, resp. C_{hnr1} is the half-saturation concentration of NO_3^- and C_{io1} the characteristic inhibition concentration of O_2 for the oxidation of POM_1 by nitrate reduction and similarly C_{hnr2} and C_{io2} are the respective constants for POM_2. Concentrations of solids are expressed in $\mathrm{kg\,(m^3\ solid\ sediment)}^{-1}$, those of solutes in $\mathrm{mol\,(m^3\ porewater)}^{-1}$; the different reaction rates, $\hat{R}$, are expressed in terms of the dissolving/remineralised solid, in $\mathrm{kg\,(m^3\ total\ sediment)}^{-1}$.

Calcite dissolution	$\hat{R}_{\mathrm{cdis}} = k_{\mathrm{c}}\,(1-\varphi)\,[\mathrm{Calcite}]\,((1-[CO_3^{2-}]/C_{\mathrm{cs}})^+)^{4.5}$
	with $k_{\mathrm{c}} = 365.25\,\mathrm{yr}^{-1}\,(= 1\,\mathrm{day}^{-1})$, $C_{\mathrm{cs}} = C_{\mathrm{cs}}(S,T,p)$
Oxic POM_1 remineralisation	$\hat{R}_{\mathrm{om1ox}} = k_{\mathrm{ox1}}\,(1-\varphi)\,[POM_1]\,([O_2]/(C_{\mathrm{hox1}} + [O_2]))$
	with $k_{\mathrm{ox1}} = 0.32\,\mathrm{yr}^{-1}$, $C_{\mathrm{hox1}} = 20\,\mathrm{\mu mol\,L}^{-1}$
POM_1 remin. by nitrate reduction	$\hat{R}_{\mathrm{om1nr}} = k_{\mathrm{nr1}}\,(1-\varphi)\,[POM_1]\,([NO_3^-]/(C_{\mathrm{hnr1}} + [NO_3^-]))\,(C_{\mathrm{io1}}/(C_{\mathrm{io1}} + [O_2]))$
	with $k_{\mathrm{nr1}} = 0.0032\,\mathrm{yr}^{-1}$, $C_{\mathrm{hnr1}} = 5\,\mathrm{\mu mol\,L}^{-1}$, $C_{\mathrm{io1}} = 20\,\mathrm{\mu mol\,L}^{-1}$
Oxic POM_2 remineralisation	$\hat{R}_{\mathrm{om2ox}} = k_{\mathrm{ox2}}\,(1-\varphi)\,[POM_2]\,([O_2]/(C_{\mathrm{hox2}} + [O_2]))$
	with $k_{\mathrm{ox2}} = 0.032\,\mathrm{yr}^{-1}$, $C_{\mathrm{hox2}} = 20\,\mathrm{\mu mol\,L}^{-1}$
POM_2 remin. by nitrate reduction	$\hat{R}_{\mathrm{om2nr}} = k_{\mathrm{nr2}}\,(1-\varphi)\,[POM_2]\,([NO_3^-]/(C_{\mathrm{hnr2}} + [NO_3^-]))\,(C_{\mathrm{io2}}/(C_{\mathrm{io2}} + [O_2]))$
	with $k_{\mathrm{nr2}} = 0.0032\,\mathrm{yr}^{-1}$, $C_{\mathrm{hnr2}} = 5\,\mathrm{\mu mol\,L}^{-1}$, $C_{\mathrm{io2}} = 20\,\mathrm{\mu mol\,L}^{-1}$
Opal dissolution	$\hat{R}_{\mathrm{odis}} = k_{\mathrm{o}}\,(1-\varphi)\,[\mathrm{Opal}]\,(C_{\mathrm{os}} - [H_4SiO_4])^+$
	with $k_{\mathrm{o}} = 0.03\,\mathrm{yr}^{-1}\,\mathrm{mol}^{-1}\,\mathrm{m}^3$, $C_{\mathrm{os}} = 1000\,\mathrm{\mu mol\,L}^{-1}$